












Article

QSAR Studies, Molecular Docking, Molecular Dynamics, Synthesis, and Biological Evaluation of Novel Quinolinone-Based Thiosemicarbazones against *Mycobacterium tuberculosis*

Jhesua Valencia ¹, Vivian Rubio ², Gloria Puerto ², Luisa Vasquez ², Anthony Bernal ¹, José R. Mora ³, Sebastian A. Cuesta ^{3,4}, José Luis Paz ⁵, Braulio Insuasty ⁶, Rodrigo Abonia ⁶, Jairo Quiroga ⁶, Alberto Insuasty ⁷, Andres Coneo ⁸, Oscar Vidal ⁸, Edgar Márquez ^{1,*} and Daniel Insuasty ^{1,*}

¹ Grupo de Investigación en Química y Biología, Universidad del Norte, Km 5 vía Puerto Colombia, Barranquilla 081007, Colombia

² Grupo de Micobacterias, Red TB Colombia, Dirección de Investigación en Salud Pública, Instituto Nacional de Salud, Bogotá 111321, Colombia

³ Grupo de Química Computacional y Teórica (QCT-USFQ), Departamento de Ingeniería Química, Universidad San Francisco de Quito, Diego de Robles y Vía Interoceánica, Quito 170157, Ecuador

⁴ Department of Chemistry, Manchester Institute of Biotechnology, The University of Manchester, 131 Princess Street, Manchester M1 7DN, UK

⁵ Departamento Académico de Química Inorgánica, Facultad de Química e Ingeniería Química, Universidad Nacional Mayor de San Marcos, Cercado de Lima 15081, Peru

⁶ Research Group of Heterocyclic Compounds, Department of Chemistry, Universidad del Valle, A. A., Cali 25360, Colombia

⁷ Grupo de Investigación en Materiales Funcionales Nanoestructurados, Universidad CESMAG, Pasto 520003, Colombia

⁸ Medicine Department, Division of Health Sciences, Universidad del Norte, Barranquilla 081007, Colombia

* Correspondence: ebrazon@uninorte.edu.co (E.M.); insuastyd@uninorte.edu.co (D.I.)



Citation: Valencia, J.; Rubio, V.; Puerto, G.; Vasquez, L.; Bernal, A.; Mora, J.R.; Cuesta, S.A.; Paz, J.L.; Insuasty, B.; Abonia, R.; et al. QSAR Studies, Molecular Docking, Molecular Dynamics, Synthesis, and Biological Evaluation of Novel Quinolinone-Based Thiosemicarbazones against *Mycobacterium tuberculosis*. *Antibiotics* **2023**, *12*, 61. <https://doi.org/10.3390/antibiotics12010061>

Academic Editor: Marcelina Mazur

Received: 20 October 2022

Revised: 21 December 2022

Accepted: 22 December 2022

Published: 29 December 2022



Copyright: © 2022 by the authors. Licensee MDPI, Basel, Switzerland. This article is an open access article distributed under the terms and conditions of the Creative Commons Attribution (CC BY) license (<https://creativecommons.org/licenses/by/4.0/>).

Abstract: In this study, a series of novel quinolinone-based thiosemicarbazones were designed in silico and their activities tested in vitro against *Mycobacterium tuberculosis* (*M. tuberculosis*). Quantitative structure-activity relationship (QSAR) studies were performed using quinolinone and thiosemicarbazide as pharmacophoric nuclei; the best model showed statistical parameters of $R^2 = 0.83$; $F = 47.96$; $s = 0.31$, and was validated by several different methods. The van der Waals volume, electron density, and electronegativity model results suggested a pivotal role in antituberculosis (anti-TB) activity. Subsequently, from this model a new series of quinolinone-thiosemicarbazone **11a–e** was designed and docked against two tuberculosis protein targets: enoyl-acyl carrier protein reductase (InhA) and decaprenylphosphoryl- β -D-ribose-2'-oxidase (DprE1). Molecular dynamics simulation over 200 ns showed a binding energy of -71.3 to -12.7 Kcal/mol, suggesting likely inhibition. In vitro antimycobacterial activity of quinolinone-thiosemicarbazone for **11a–e** was evaluated against *M. bovis*, *M. tuberculosis* H37Rv, and six different strains of drug-resistant *M. tuberculosis*. All compounds exhibited good to excellent activity against all the families of *M. tuberculosis*. Several of the here synthesized compounds were more effective than the standard drugs (isoniazid, oxafloxacin), **11d** and **11e** being the most active products. The results suggest that these compounds may contribute as lead compounds in the research of new potential antimycobacterial agents.

Keywords: *Mycobacterium tuberculosis*; QSAR; docking; quinolinone; thiosemicarbazone; molecular dynamics and cytotoxicity

1. Introduction

Tuberculosis (TB), also known as phthisis, is a chronic severe infectious disease caused by *Mycobacterium tuberculosis* that affects humans [1]. TB continues to be a serious global

health problem, and before the coronavirus pandemic (COVID-19) it was the main cause of death from an infectious agent, being more deadly than HIV [2]. TB worldwide mortality data show that more than one million people die from this single pathogen annually: TB causes an estimated 10 million new cases and around 1.8 million deaths per year [3]. Moreover, it has been reported that approximately one-quarter of the world population shares the TB infection in a latent phase, representing a high-risk population susceptible to future active TB infection [4]. High morbidity, mortality, and the emergence of new resistant TB strains make this disease a constant source of biomedical research; therefore, a cure for TB has been listed as one of the main goals of the World Health Organization [5,6]. Control of TB in most of the world relies on diagnostics tests such as microscopic-based diagnostics with very low sensitivity and a very old vaccine (Bacille Calmette–Guérin; BCG) and finally, very old therapeutics [7]. Hence, multidrug-resistant (MDR) TB is a growing risk for the population worldwide, with increasingly favorable conditions for the bacteria including the HIV epidemic, other comorbidities such as type 2 diabetes, and low-quality life condition in lower and middle-income countries [5,8].

On the other hand, TB chemotherapy involves first-line oral drugs such as isoniazid, ethambutol, pyrazinamide, and rifampicin for approximately six months; in the first two months of the treatment, all four chemicals are applied, whereas in the last two months, only two antituberculosis (anti-TB) drugs are used: isoniazid and rifampicin. Antibiotic resistance requires a different treatment with second-generation therapeutics [8]. Unfortunately, new TB strains develop resistance to first and second generation [9]. As a result, morbidity and mortality are higher in immunosuppressed HIV patients [10]. Furthermore, the lack of therapeutic adherence due to the long treatment time causes TB-infected patients to abort the treatment, which could increase the resistance of some TB strains [8,11].

The search for new antimicrobial compounds has become a worldwide goal shared by multidisciplinary teams. Recently, bioinformatics teams have focused on compounds designed in silico, thus allowing the discovery of new molecular targets without the experimental laboratory phase. Compound discovery requires investigating the structural features of a compound and its interaction with the cellular pathways that allow it to induce or block a specific human disorder pathway/pathogen. For example, there is a lack of compounds that could deliver efficient results against the TB epidemic; consequently, research and the generation of new chemicals are paramount in the war against TB [11,12]. Novel research could lead to the discovery of several compounds with a high probability of targeting suitable molecules, avoiding the synthesis of inactive compounds and clinical assays, thus reducing the compound discovery time. The different in silico methods, such as quantitative structure-activity relationship (QSAR) and molecular docking, play an essential role in gaining this prior knowledge in compound discovery endeavors [13,14].

In recent years, several compounds have been designed based on cheminformatic tools such as QSAR (quantitative structure-activity relationship) and molecular docking [15,16]. Moreover, additional works have proved that employing these techniques enhances the probability of finding new anti-TB structures, with more probability of success than using only chemical intuition, and further reducing investigation time and costs [17].

Tuberculosis-related literature suggests the *N*-heterocyclic structures are ideal pharmacophoric scaffolds for anti-TB molecules [18,19]. Moreover, the quinolones and their oxo-derivatives are the principal functional group for several drugs used as second-line antibiotics against tuberculosis, among them, bedaquiline **1** [20], ofloxacin **2** [21], gatifloxacin **3** [22], and norfloxacin **4** [23], used for the treatment of MDR-TB, and other structures such as **5** [24], **6** [25], and **7** [26] are reported as promising inhibitors of *M. tuberculosis* H37Rv (Figure 1). Furthermore, it has been shown that the thiosemicarbazide nucleus allows the generation of compounds with a broad pharmacological spectrum; specifically, thiosemicarbazones have various biological characteristics such as antitumor [27], antiprotozoal [28], antiviral, and antibacterial [29], and their anti-TB properties stand out [30]. For example, hybrids such as quinoline–thiosemicarbazones **8** [31], benzaldehyde thiosemicar-

bazones **9** [32], and thiosemicarbazones **10** [33] have been reported as excellent inhibitors of *M. tuberculosis*.

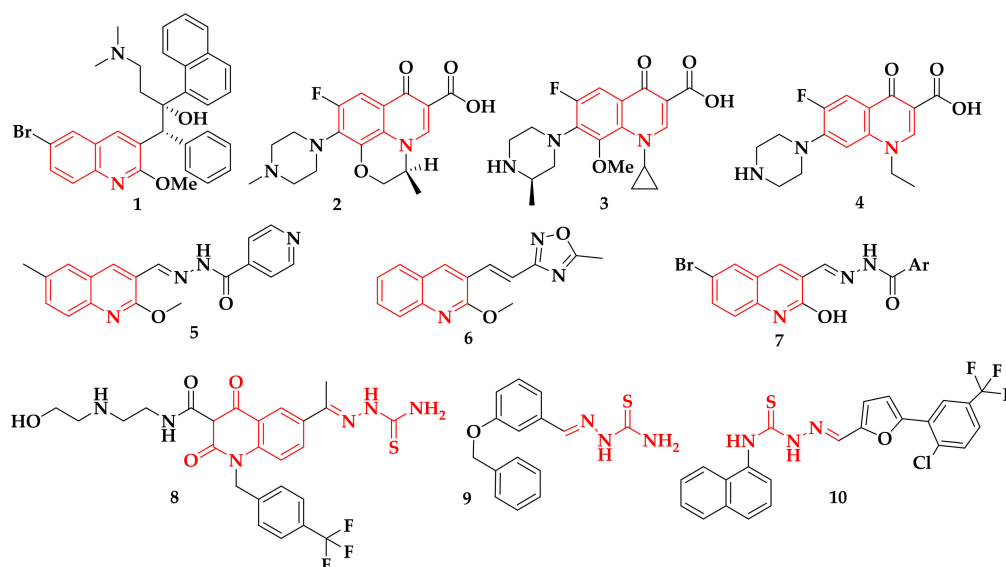


Figure 1. Structure of quinolinone-based anti-TB drugs: quinolines, quinolones, and thiosemicarbazones, used as inhibitors of *M. tuberculosis* H37Rv.

In addition, different possible tuberculosis protein targets were reported for these structures, representing a real opportunity to design new compounds with other mechanisms of action, which are a cornerstone to fight against tuberculosis resistance to the current antibiotics [9,34–40].

Considering the exceptional anti-TB activity of the scaffolds mentioned above, it seems attractive to link both structures, quinolinone and thiosemicarbazide moieties, and prove their potential anti-TB activity. In this sense, this research reports the synthesis of new quinolinone–thiosemicarbazone hybrids and their anti-TB activity evaluation, designed using the combination of quantitative structure-activity relationship (QSAR), molecular docking, and molecular dynamic (MD) studies. Furthermore, the mathematical models herein guided the design of five new compounds that were synthesized and exhibited potent anti-TB in vitro activity against *M. tuberculosis*.

2. Results and Discussion

2.1. QSAR Modeling

The minimum energy structures for molecules depicted in Figure 16 (see Section 3) were calculated using Gaussian 16. The minimum energy structures were confirmed using frequency calculation with no negative frequency for all data. In this regard, molecular descriptors were computed using these minimum energy structures together with the anti-TB activity (pMIC). Several multiparametric models were generated using molecular descriptors as independent variables and pMIC as a dependent variable (response variable). The most significant ones are shown in Equations (1)–(3), respectively.

$$\text{pMIC} = 5.579 + 33.968(11\mathbf{a}) + 2.791(8\mathbf{a}) + 0.100(13\mathbf{a}) - 0.121(75\mathbf{a}) - 0.275(24\mathbf{a}) - 12.865(63\mathbf{a}) - 13.927\chi \quad (1)$$

$$r = 0.95, r^2 = 0.91, F = 36.10, \sigma = 0.32, Q_{\text{LOO}} = 0.83$$

$$\text{pMIC} = 6.048 + 2.877(8\mathbf{a}) + 0.065(17\mathbf{a}) - 0.258(24\mathbf{a}) - 7.041(63\mathbf{a}) - 18.108\chi \quad (2)$$

$$r = 0.92, r^2 = 0.86, F = 31.92, \sigma = 0.31, Q_{\text{LOO}} = 0.77$$

$$\text{pMIC} = 6.401 + 2.877(8\mathbf{a}) - 0.228(24\mathbf{a}) - 19.793\chi \quad (3)$$

$$r = 0.91, r^2 = 0.83, F = 47.96, \sigma = 0.31, Q_{\text{LOO}} = 0.78$$

where: **1a** = P2_B_AB_nCi_2_SS7_A_KA_m-e_MAS; **8a** = SD_B_AB_nCi_2_SS8_LGP [2-4]_v-c_MAS; **13a** = RA_Q_AB_nCi_2_SS8_T_KA_h_MAS; **24a** = K_B_AB_nCi_2_NS4_P_KA_e-c_MAS); **34a** = RA_Q_AB_nCi_2_MP1_P_NSRW_s_MAS; **37a** = P2_B_AB_nCi_2_SS4_X_LGP [1,2,6]_c-p_MAS; **11a** = P2_B_AB_nCi_2_SS5_X_LGP [1;2;6]_c-m_MAS; **60a** = Q3_B_AB_nCi_2_SS1_P_LGP [1]_m-h_MAS; **62a** = I50_F_AB_nCi_2_SS7_T_LGP [1]_h_MAS; **63a** = Q2_B_AB_nCi_2_SS5_P_LGP [4-6]_v-c_MAS; **75a** = I50_B_AB_nCi_2_SS1_T_LGP [1,2,6]_v-h_MAS; **88a** = Q1_F_AB_nCi_2_SS6_P_NSRW_c_MAS; χ = molecular electronegativity, r^2 = correlation coefficient, F = Fisher coefficient, σ = standard deviation, and Q_{LoO} = predictability coefficient (leave-one-out cross-validation).

Data analysis revealed that although all generated models were statistically significant, model 3 presented the best combination between statistics and the number of attributes (only three), allowing better handling and interpretation. Therefore, this model was selected for further analysis and to guide the design of new potential anti-TB compounds. The selected model was used to predict biological activity values for a training set of 23 compounds (71.87%) and a prediction set of 9 compounds (28.21%). Figure 2 shows the excellent correspondence between experimental and predicted values for anti-TB activity.

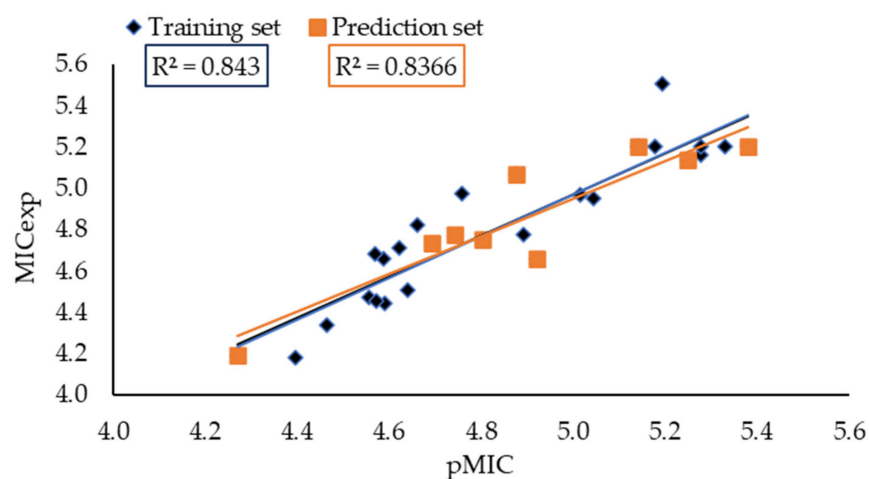


Figure 2. Correlation between experimental and predicted anti-TB activity values.

In addition, Table S1 (in Supplementary File) shows the values of MIC_{exp}, pMIC, their residuals, the corresponding value obtained from model 3, and the difference between MIC_{exp} and Q_{LoO} . A linear trend is observed in both diagrams, indicating an excellent internal prediction of model 3. Moreover, the plot of residues vs MIC_{exp} and Q_{LoO} residues vs MIC_{exp} demonstrates that residues are uniformly closed to zero, corroborating the absence of consequential errors in the amount obtained. Finally, the Pearson correlation between the attributes for model 3 was calculated and is shown in Table 1. According to these results, there is no collinearity between the molecular descriptors present in Equation (3), demonstrating that the equation is not redundant, with attributes independent of each other [41].

Table 1. Pearson correlations obtained for model 3.

Attribute	8a	24a	χ
8a	1	0.02	−0.51
24a	0.02	1	0.25
χ	−0.51	0.25	1

2.2. Applicability Domain (AD)

The applicability domain analysis was used to detect outliers on the test set and provide reliable and accurate predictions. In this study, the AD was estimated utilizing a

William diagram [42]. In this procedure, the leverage threshold ($h^* = 0.5217$) was considered; therefore, a score greater than 0.5217 was used as the criteria to identify if a compound was outside the AD. According to Figure 3, compound 26 fell outside the application domain; therefore, it was removed from the model for future analysis. Thus, according to this AD, the model obtained can be used as a guide for designing hybrids based on quinolines with anti-TB properties since it has a reliable prediction and high confidence [43].

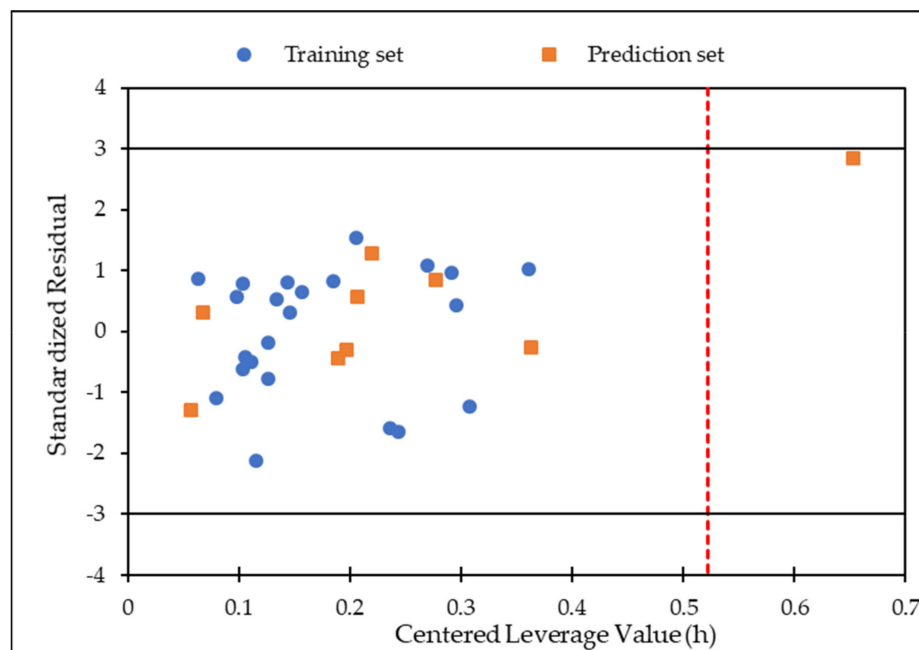


Figure 3. Applicability domain plot of standardized residuals versus centered leverage value of model 3.

2.3. External Validation of the Model QSAR

In Table 2, the different statistical values of the predictive capacity of QSAR model were obtained using the leave-one-out cross-validation (Q_{LOO}), leave many out cross-validation (Q_{LMO}), Y-randomization test, and bootstrap (Q_{boot}). Meanwhile, a r^2 close to 1 means a good fit for the model; the values of Q_{LOO} , Q_{LMO} , and Q_{boot} indicate that the obtained model has high predictability since they have a validation value greater than 0.5 [44]. In addition, Y-scrambling values, 0.1367 for $a(R^2)$ and -0.2774 for $a(Q^2)$, suggest the statistical model does not correlate by chance.

Table 2. Different statistical values of the predictive capacity of QSAR model 3.

Size	r^2	Q_{LOO}	Q_{LMO}	Q_{ext}	Q_{boot}	$a(R^2)$	$a(Q^2)$	F
3	0.83	0.78	0.72	0.81	0.716	0.13	-0.27	47.96
$pMIC = 6.401 + 2.877(8a) - 0.228(24a) - 19.793\chi$								

In addition, Tropsha's test validates [45] and the accuracy of predicting pMIC values for model 3. This model met all the test requirements, suggesting an accurate prediction (Table 3).

Table 3. Validation based on the Tropsha's test for QSAR model 3.

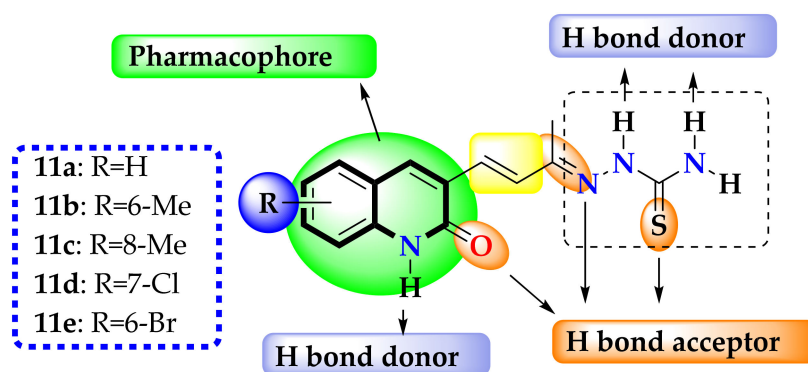
Criterion	Leave-One-Out Validation		External Validation	
	Result	Assessment	Result	Experimental
$r^2 > 0.6$	0.83	PASS	0.83	PASS
$r^2_{\text{val}} > 0.5$	0.78	PASS	0.81	PASS
$(r^2_{\text{val}} - r^2_0)/r^2_{\text{val}} < 0.1$	0.00	PASS	0.00	PASS
$(r^2_{\text{val}} - r^2_0)/r^2_{\text{val}} < 0.1$	0.06	PASS	0.00	PASS
$\text{abs}(r^2_0 - r'^2_0) < 0.1$	0.05	PASS	0.00	PASS
$0.85 < K < 1.15$	0.99	PASS	0.99	PASS
$0.85 < K' < 1.15$	0.99	PASS	1.00	PASS

As it can be noted, all of the standard statistical procedures used in this work validate model 3 as a robust, meaningful, and predictable model; therefore, this will operate as a guide for the design of new molecules with potential anti-TB activity.

2.4. Design of the Structures

Model 3 indicates that the anti-TB activity might be related to van der Waals descriptors. The parameter has a positive value in the equation, which means that the more positive this descriptor is, the higher the biological activity. The second coefficient in the equation is related to electron density; this descriptor's negative value and magnitude suggest a slight decrease in activity as electron density increases. Finally, the last descriptor is molecular electronegativity; the sign and magnitude suggest decreased activity as electronegativity increases. Considering the importance and the kind of descriptors involved in the QSAR model 3, it started from the most active structure (26, Figure 16), and some modifications were made to find new potential anti-TB compounds.

An important factor to take into account is the free rotation and electronegativity of the atoms present in the thiocarbamide group; free rotation increases the molecular volume, which, according to Equation (3), favors biological activity; on the other hand, the presence of N and S makes the electron density and, therefore, the molecular electronegativity, sensitive to the substituents in this molecular region, which, according to Equation (3), would decrease the biological activity. In this sense, the modifications were focused on the quinoline ring. For the structural change, the simplest isosteric substituents reported in the literature were used and are shown in Figure 4 [46]: H, CH₃, Cl, and Br.

**Figure 4.** Pharmacophore and QSAR-based designed compounds in this work.

Substitution by methyl groups at positions 6 and 8 slightly decreased the biological activity, while the Cl and Br substituents increased it considerably. This is because the methyl group, which is an electron-donor group, increased the molecular electronegativity and therefore decreased the biological activity. In contrast, the Cl and Br groups, which are electron-withdrawing groups, increased the molecular volume and reduced the molecular

electronegativity; therefore, the biological activity was increased in these two compounds (**11d** and **11e**, Table 4).

Table 4. Molecular descriptor values and minimum inhibitory concentration predicted for five compounds designed using the QSAR model obtained herein.

Comp.	R	Y_p	MIC_p (μM)	8a	24a	χ	HD	HA	P	MW
11a	H	5.49	0.23	0.25	−2.29	0.10	3	3	−0.12	286.35
11b	6-Me	5.56	0.22	0.23	−3.02	0.11	3	3	0.97	300.38
11c	8-Me	5.93	0.10	0.54	−0.93	0.11	3	3	0.97	300.38
11d	7-Cl	6.82	0.14	0.57	−4.26	0.11	3	3	1.34	320.80
11e	6-Br	7.03	0.09	0.57	−4.99	0.10	3	3	1.49	365.25

8a = (SD_B_AB_nCi_2_SS8_P_LGP [2,3,4] v-c_MAS); 24a = (K_B_AB_nCi_2_NS4_P_KA_e-c_MAS); χ = electronegativity; HD = donor H; HA = acceptor H; P = coefficient partition; MW = molecular weight.

Table 4 shows the molecular descriptors for the designed compounds according to the selected QSAR model. The values of some parameters used in Lipinski's [47] rule are also shown. As it can be noted, all of the proposed compounds are potentially active against H37Rv anti-TB strains and meet Lipinski rules.

2.5. Molecular Orbitals

In the case of antimicrobial activity, several reports suggest structures with, at least, a frontier orbital located in a specific molecular region displaying a broad spectrum of activity [48–57], compared to compounds whose frontier orbitals are scattered in the whole structures. This latter characteristic is related to the compound fluorescence ability [58–60]. In addition, at least one of the two characteristics pointed out above are presented in the anti-TB compounds already reported [58,61–63].

According to Figure S2, the designed compounds could be divided in two kinds: the first one, corresponding to compounds **11b** and **11c**, exhibiting the HOMO (highest energy occupied orbital) and LUMO (unoccupied orbital of lower energy) distributed among all the structure; in this sense, these compounds might act as nucleophilic (hydrogen acceptor) or electrophilic (hydrogen donor) with the biological target by using both quinolinone and thiosemicarbazide parts on the molecule. In contrast, in the second kind, the electron-withdrawing substituents shift the HOMO to the thiosemicarbazone moiety. In line with these results, the designed compounds meet some characteristics in agreement with the already reported anti-TB compounds. Moreover, compounds **11d** and **11e** exhibited the HOMO shape more closely than nitro-substituted 1,3-benzothiazoles (BTZ043), a compound family inhibiting the DprE1 protein. These results confirm that the designed compounds meet the electronic characteristic to become molecules potentially active against *M. tuberculosis*.

2.6. Molecular Docking

A molecular docking procedure was carried out to find additional evidence supporting the results obtained from the QSAR method related to the potential antimycobacterial activity of the designed compounds.

In this work, several proteins reported as targets of quinolines and quinolones were evaluated: DNA-gyrase, enoyl-acyl carrier protein reductase, and ATP-synthase [64–67]; in Table 5 the target with the best scoring values for the designed compounds are shown. The selection criteria were based on the average scoring values for the designed compounds in each protein jointly in comparison with the inhibitor reported for each protein.

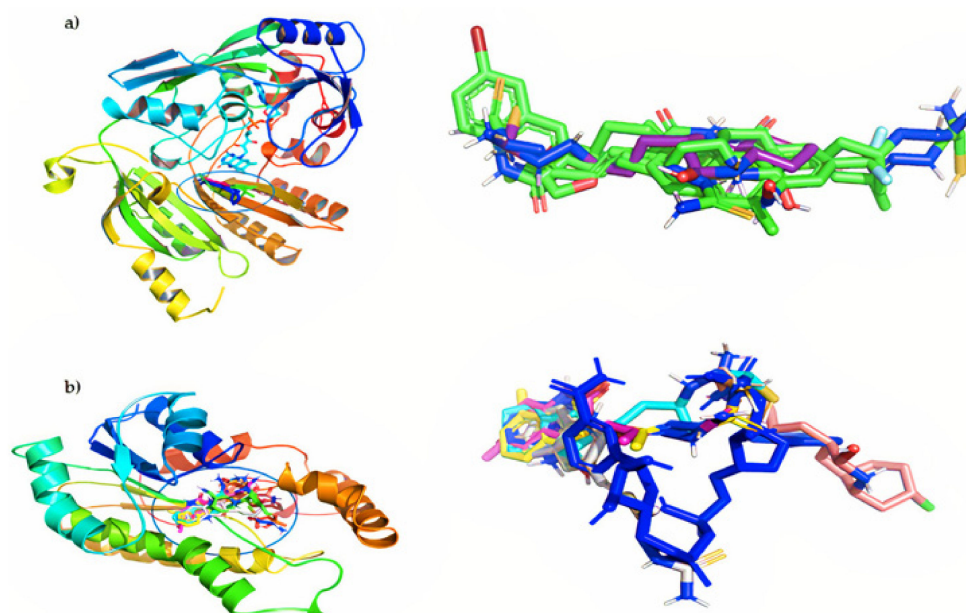
Table 5. Vina scores were obtained for the designed compounds and the reported target inhibitors.

Compounds	Vina Score (kcal/mol)	RMS	RMS	
		DPrE1	InhA	
11a	−7.30	1.8	−7.60	2.3
11b	−7.10	2.4	−8.20	1.8
11c	−7.50	1.6	−8.40	1.5
11d	−7.20	2.0	−8.40	1.3
11e	−7.90	1.5	−8.50	1.2
BTZ043	−10.70	1.3	−8.30	2.4
INH-NADP complex	−6.6	1.5	−10.40	0.8

The protein decaprenylphosphoryl- β -D-ribose-2'-oxidase (DprE1) was also evaluated, given recent interest in it as a fundamental target for developing new antituberculosis compounds because of the structural similarity between its inhibitors and the compounds designed in this research [68].

Table 5 shows a vina score for the designed compounds against proteins InhA and DprE1, which present the best scoring of the designed compounds. The finding of vina score values lower than 5 suggests the possible formation of complexes between the compounds and the selected proteins. According to the obtained results, the designed compounds present suitable affinity towards both proteins, with compounds 11d and 11e having the best performance against both studied proteins.

As shown in Figure 5, all compounds hit the target at the active site. Furthermore, they overlapped the area of action of the compound reported as an inhibitor in each case, with root mean square deviation (RMSD) values less than 3 Å. Finally, to obtain more insight into the role of molecular interaction in the ligand–receptor complexes, the molecular interaction for the co-crystallized protein was compared with the 11e protein complex obtained in each case. The respective 2D diagrams are shown in Figure 6.

**Figure 5.** Binding orientation for the most active poses: (a) left, DprE1; right, overlap of the studied compounds with the co-crystallized inhibitor (BTZ043, blue); (b) left, InhA; right, the overlay of all studied compounds with the co-crystallized inhibitor (INH-NADP, blue).

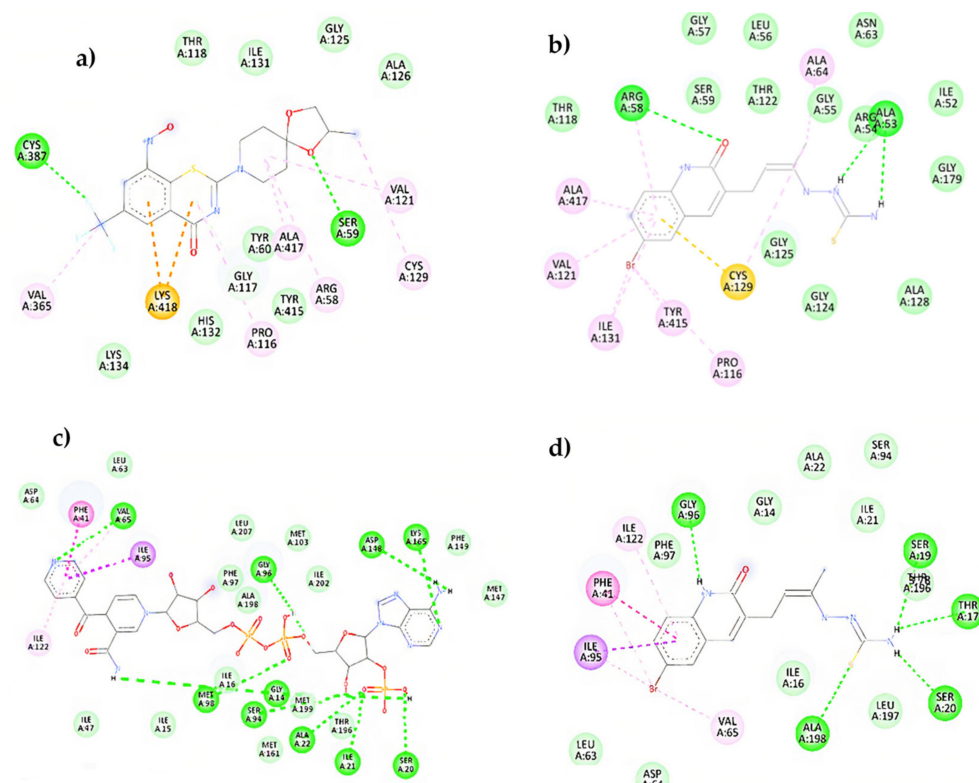


Figure 6. Two-dimensional molecular interaction diagram: (a) BTZ043-DprE1 complex; (b) **11e**-DprE1; (c) INH-NADP-InhA complex; (d) **11e**-InhA complex.

According to Figure 6, compound **11e** interacts with the DprE1 protein analogous to that of the co-crystallized inhibitor (BTZ043). The analysis of molecular interactions in the co-crystallized protein DprE1 suggests that the compound BTZ043 inhibits it mainly by van der Waals interactions where the hydrogen bonds with amino acids Cys387 and Ser59 stand out; these amino acids were reported as fundamental ones in the DprE1 inhibition [69].

In addition, the presence of a π -sulfur interaction (Lys438) can be noted; a strong hydrophobic interaction (Figure 6a). Similarly, in Figure 6b, compound **11e** presents the formation of several van der Waals interactions, such as hydrogen bonds (Arg58, Arg54, and Ala53) and a strong π -sulfur type interaction (Cys129). These results show that compound **11e** presents the same interactions as the co-crystallized inhibitor but forms different residues within the catalytic pocket. On the other hand, Figure 6c,d shows the molecular interactions between the InhA-NADP complex and compound **11e** with the active site of the InhA protein, respectively. It can be noted that the inhibition of this protein by the Inha-NADP complex takes place mainly through dipolar hydrogen bond-type interactions. However, some hydrophobic interactions are essential, such as the formation of π - π bonds and σ - π with amino acids Phe43 and Ile95, respectively.

Interestingly, compound **11e** interacted with the active site of the InhA protein in a similar way to the co-crystallized inhibitor. In this regard, hydrogen bonds with amino acids Ala198, Ser19, Ser20, Thr17, and some significant hydrophobic interactions with amino acids Phe43 (π - π) and Ile95 (π - σ), respectively, can be highlighted. In general, compound **11e** showed excellent values in its vina score and molecular interactions similar to InhA and DprE1 inhibitors already reported, suggesting its potential activity against tuberculosis. Finally, it is noteworthy that the 2D interaction diagrams contrast with the molecular orbitals, indicating that for compound **11e**, the thiosemicarbazone fragment has a fundamental role in forming hydrogen bridges. At the same time, the quinolinone moiety would favor hydrophobic interactions with significant energy.

2.7. Molecular Dynamics

To evaluate the stability of the complexes formed from the docking calculation and obtain insights into the different interactions that make possible the stability or the lack of it, a 200 ns molecular dynamics simulation was performed for **11c**, **11d**, and **11e** complexes with enoyl-acyl reductase and DprE1 targets. The potential energy, temperature, pressure, volume, and water box size were evaluated to ensure the dynamics ran correctly and reproduced reliable results. For the ligand-enoyl-acyl reductase complexes, the RMSD of the enzyme and the ligands were assessed during 200 ns of simulation (Figure 7).

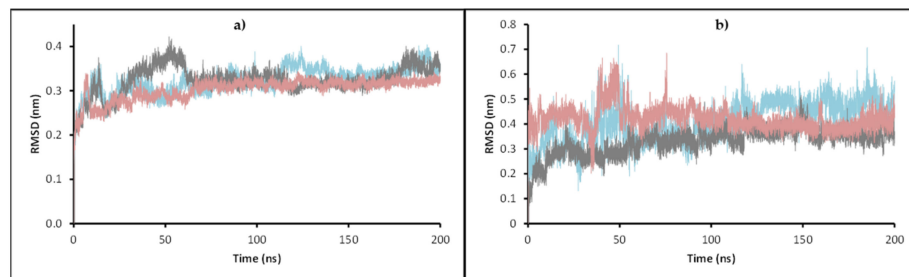


Figure 7. RMSD of enoyl-ACP reductase (a) and RMSD of the ligands (b) during the 200 ns simulations: **11c** is present in cyan, **11d** in gray, and **11e** in pink.

The results show that the enoyl-ACP reductase reached an equilibrium after 60 ns of simulation at a RMSD value of around 0.3 nm for the three systems. This result suggests that the enzyme does not experience significant conformational changes when interacting with the ligands, which may indicate the possibility of positive interaction with them, translating into a potential inhibition of the enzyme. Analyzing the RMSD of the ligands, values below 0.7 nm were found, which supports the reliability of the docking results previously found. Furthermore, low RMSD values also suggest that the complex formed presents a good stability over time, which supports the possible inhibition. A close inspection at the final step over 200 ns simulation showed that the three ligands stayed in the active site, overlaying between them and with the ligand present in the experimental crystal structure (Figure 8).

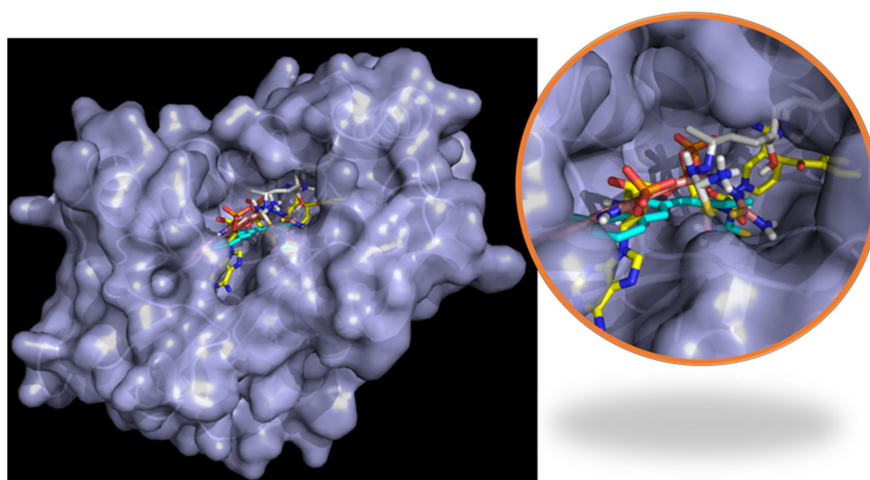


Figure 8. Final pose of **11c** (cyan), **11d** (gray), and **11e** (pink) after the 200 ns compared with (4S)-isonicotinic-acetyl-nicotinamide-adenine dinucleotide (yellow) present in the ligand in enoyl-acyl reductase (blue) crystal structure.

To obtain insights on the strength of the interactions, the number of hydrogen bonds (HBs), and the interaction energies (Coulomb and Lennard-Jones) were obtained for the system during the whole length of the simulation (Figure 9).

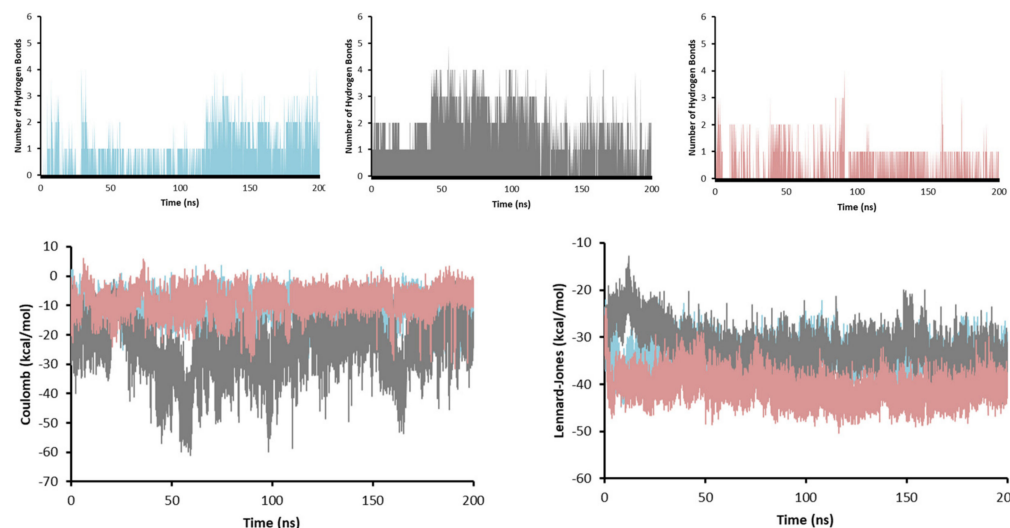


Figure 9. Number of hydrogen bonds, and Coulomb and Lennard-Jones energies **11c** (cyan), **11d** (gray), and **11e** (pink) in complex with InhA during the 200 ns of simulation.

The number of HBs is a good indicator of how strong the ligand–receptor interaction is. As more HBs are formed, the more stable the complex will be. In this sense, compound **11d** is the one that may create the most potent interaction with enoyl-acyl reductase, because it formed up to five HBs. Compound **11c** formed up to 4 HBs, 1 HB being the most abundant throughout the simulation and between 2 and 3 HBs in the last 75 ns of simulation (when it reaches equilibrium). For compound **11e**, although it also managed to make 4 HBs, only 1 HB was present during most of the simulation. These results agree with the Coulomb energy profile, where compound **11d** presented the most negative values (around -40 kcal/mol) compared to compounds **11c** and **11e**, which gave an average value of -10 kcal/mol. The Lennard-Jones potential was similar for the three molecules with values between -30 kcal/mol and -40 kcal/mol suggesting the mode of interaction between the three ligands and enoyl-acyl reductase was similar, which is expected for an inhibition behavior.

The last point of the simulation was analyzed and compared to the (4S)-isonicotinic-acetyl-nicotinamide-adenine dinucleotide interaction in the experimental crystal structure (Figure 8) to obtain more insight into the interaction between the ligands and the enoyl-ACP reductase. In the co-crystal structure (Figure 10a), the dinucleotide formed five HBs with Ile21, Asp64, Val65, Lys165, and Ile194. Furthermore, it had hydrophobic interactions with Ile95, Ile122, and two π - π interactions with Phe43 and Phe149. On the other hand, compound **11c** (Figure 10b) showed 2 HBs (Gly14, and Ser94) and 2 hydrophobic interactions (Ile16 and Phe97); compound **11d** (Figure 10c) only formed 2 HBs (Ile95, Gly96); and compound **11e** (Figure 10d) 1 HB (Met98) and 1 hydrophobic (Ile95). The dinucleotide managed to form more interactions than the tested ligands, although this was due to the most significant size of the molecule.

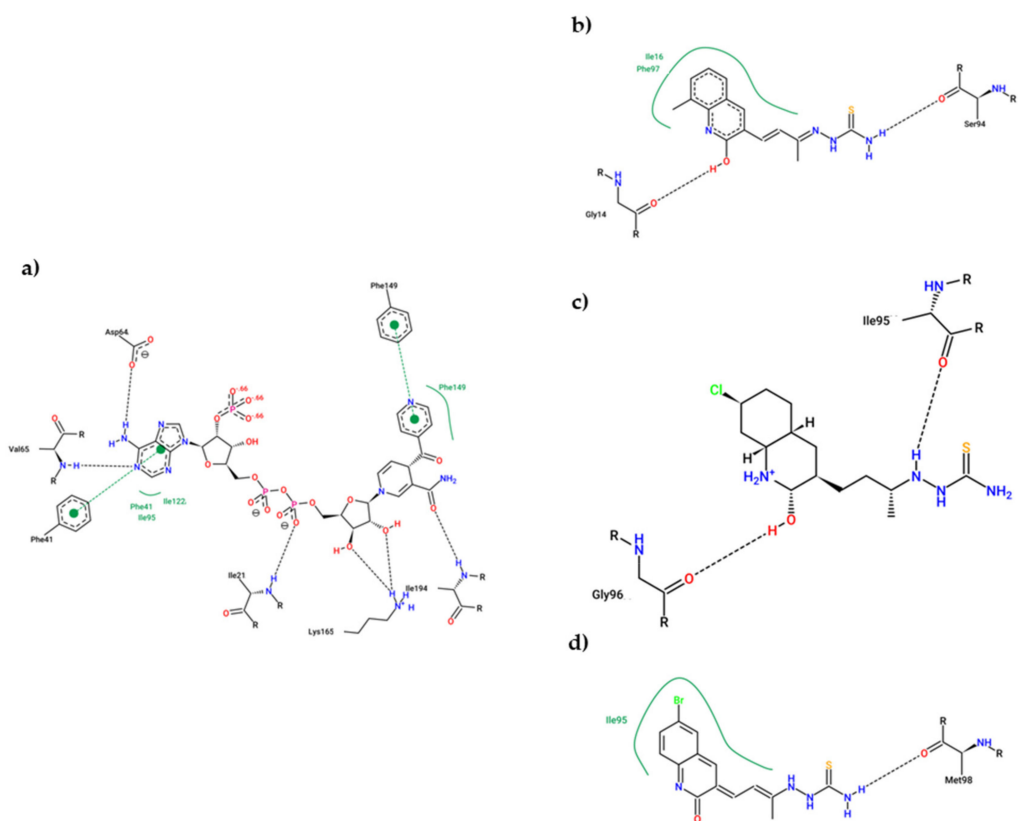


Figure 10. 2D Representation of the interaction between enoyl-acyl reductase and (4S)-isonicotinic-acetyl-nicotinamide-adenine dinucleotide (a), **11c** (b), **11d** (c), and **11e** (d).

On the other hand, similar to enoyl-acyl reductase, the DprE1-ligand complexes were evaluated by employing a molecular dynamics procedure, monitoring the results at a different time, and checking their behavior in the potential energy minimization, water box size, the temperature, the pressure, and the volume of the system during the 200 ns. Therefore, these parameters indicated a correct simulation throughout the calculation time, and the different results obtained were analyzed.

First, the pose after the simulation was assessed to see if the ligands managed to stay in the active site or if the interaction was not strong enough and the ligands left the system. DprE1 complex presents an extensive and solvent-accessible active site pocket that allows the entry of FAD and the ligand (Figure 11a). Interactions in open, active sites are less than those in close pockets, requiring stronger interactions to keep the ligand inside. For the three systems studied, the ligands and FAD managed to stay in the active site after the simulation time, suggesting a strong interaction between them and DprE1. Looking at the final pose of FAD in the three systems, their structure was overlaid with FAD in the experimental form (Figure 11b). This result was expected because cofactors-enzyme complexes are very stable.

Furthermore, due to FAD's large size, which manages to penetrate deep inside the enzyme, and the multiple functional groups that can quickly form hydrogen bonds with the enzyme, a stable and robust interaction was very likely to be developed, constraining its movement. On the other side, comparing the final pose of the ligand in the active site with the experimental one found in 6HEZ, a good overlay was not found, although they managed to stay inside the pocket (Figure 11c). This behavior was probably related to the lack of interactions between the ligand and the enzyme. Still, the few interactions with the enzyme and possible interactions with the cofactor may be strong enough to keep the ligand in the active site inhibiting the enzyme.

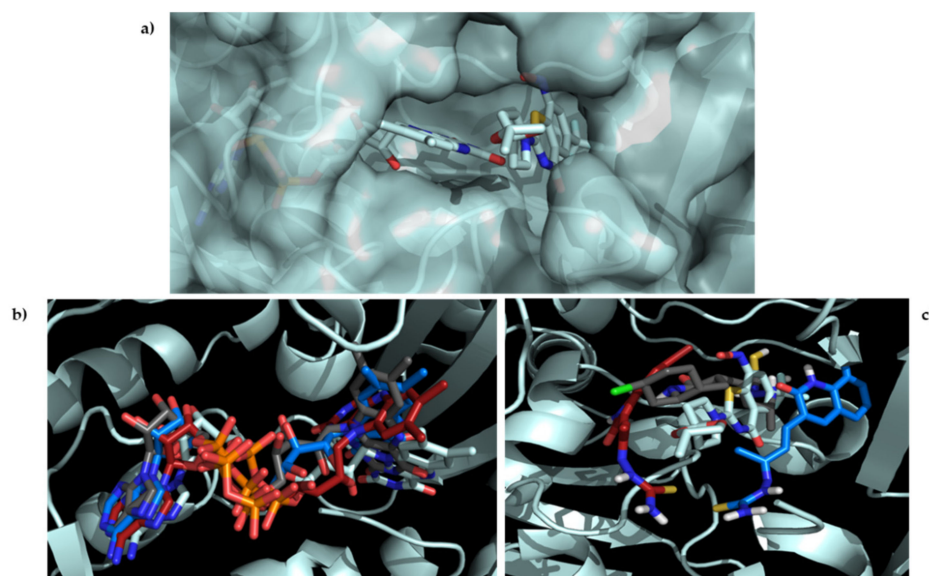


Figure 11. Experimental pose of FAD and BTZ043 in the experimental structure of (a) FAD (b) and ligands; (c) final pose after the 200 ns compared with DprE1. DprE1 and its ligands are presented in pale cyan, **11c** in blue, **11d** in gray, and **11e** in red-pink.

RMSD of the ligands (Figure 12) shows that compound **11c** had a significant change in its conformation compared to the result of the docking calculation. Still, values did not reach 0.3 nm in any of the systems, suggesting good stability in the enzyme–ligand complex. For ligands **11d** and **11e**, their RMSD values were less than 0.15 nm during most simulation time. For DprE1 in the three complexes, values were very similar, between 0.3 nm and 0.5 nm, during the simulation. In system **11e**, a peak was observed at 130 ns, suggesting a particular distortion that disappeared in the last 50 ns of simulation where the RMSD kept stable; therefore, the ligands studied do not produce critical conformational changes to the enzyme, indicating a similar binding mode to that of the co-crystallized ligand. In addition, short-range Coulomb and Lennard-Jones energies were obtained throughout the simulation (Figure 13) to complement the stability analysis of the complex studied.

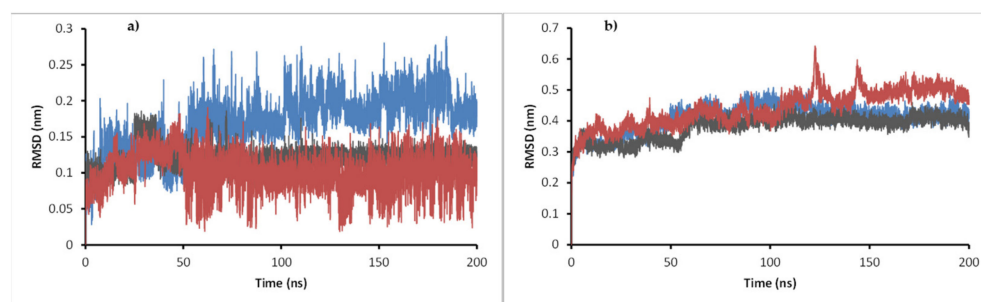


Figure 12. (a) RMSD of compounds **11c**, **11d**, **11e** in complex with DprE1. (b) RMSD of the enzyme in each complex during the 200 ns simulations. **11c** is present in blue, **11d** in gray, and **11e** in red.

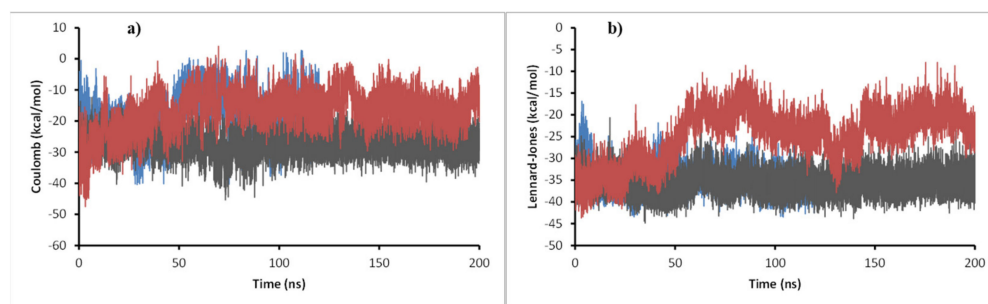


Figure 13. (a) Coulomb energy plot and (b) Lennard-Jones short-range energies of **11c** (blue), **11d** (gray), and **11e** (red) in complex with DprE1 during the 200 ns of simulation.

As shown in Figure 14, all energies were negative, indicating a suitable attractive interaction between ligands and the target. Regarding Coulomb energies, compound **11c**'s energy was 10 kcal/mol lower than that of the other two compounds, suggesting a more robust interaction. For Lennard-Jones potential, **11c** and **11d** presented a similar profile with values around -35 kcal/mol, while **11e** energy stabilized during the second half of the simulation at around -20 kcal/mol.

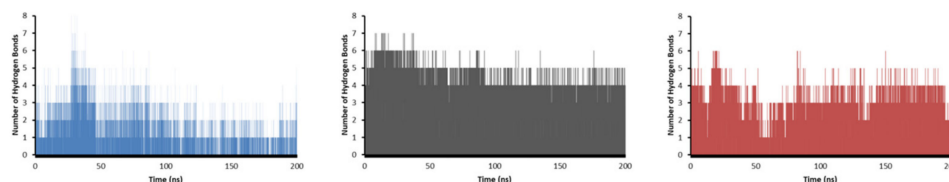


Figure 14. The number of hydrogen bonds for **11c** (blue), **11d** (gray), and **11e** (red) in complex with DprE1 during the 200 ns of simulation.

Finally, a hydrogen bond (HB) analysis was performed on the three systems (Figure 14). The results showed that **11d** was the ligand that formed the more significant number of HBs during most of the simulation, followed by **11e**, and at the end **11c**, which agrees with the most negative values found in Coulomb and Lennard-Jones energies. During the 200 ns simulation, **11d** managed to form 4 HBs throughout the simulation, becoming 5 in more than half the time. Furthermore, **11d** formed 6 and even 7 HBs during a short period. For **11e**, 3 HBs were created during most simulation time, with 6 HBs the highest, but only for a short time. Finally, **11c** formed only 1 HB in the simulation, while 2 and 3 HBs were formed after half of the time. Interestingly, although it was the compound with the least number of HBs during the simulation, at one point of the calculation, it created 8 HBs, which was the highest of all the systems.

The 2D representation of the final conformation of the complex was analyzed to see which residues were the most important for the interaction (Figure 15). The interactions between FAD and DprE1 were also plotted and HBs with 14 different amino acids were found, explaining the stability of FAD during the simulation. For BTZ043 (experimental), there was one HB with Lys438 and hydrophobic interaction with Val365 where the trifluoro group is located. Compound **11c** presented three interactions; 2 HBs (His315 and Leu317), and 1 hydrophobic interaction with Val365. Compound **11d** showed only 2 HBs; with Gln336 and Lys438, while **11e** had only 1 HB with Thr118. Along with the HBs, any interaction with FAD may also help the stability and inhibit DprE1. Therefore, distances between the different ligands and FAD were measured. Compound **11d** presented the shortest average distance (2.3 Å), followed by **11e** (3.7 Å), and **11c** (7.5 Å). The distance between ligand BTZ043 and FAD for the experimental crystal structure was 4.5 Å.

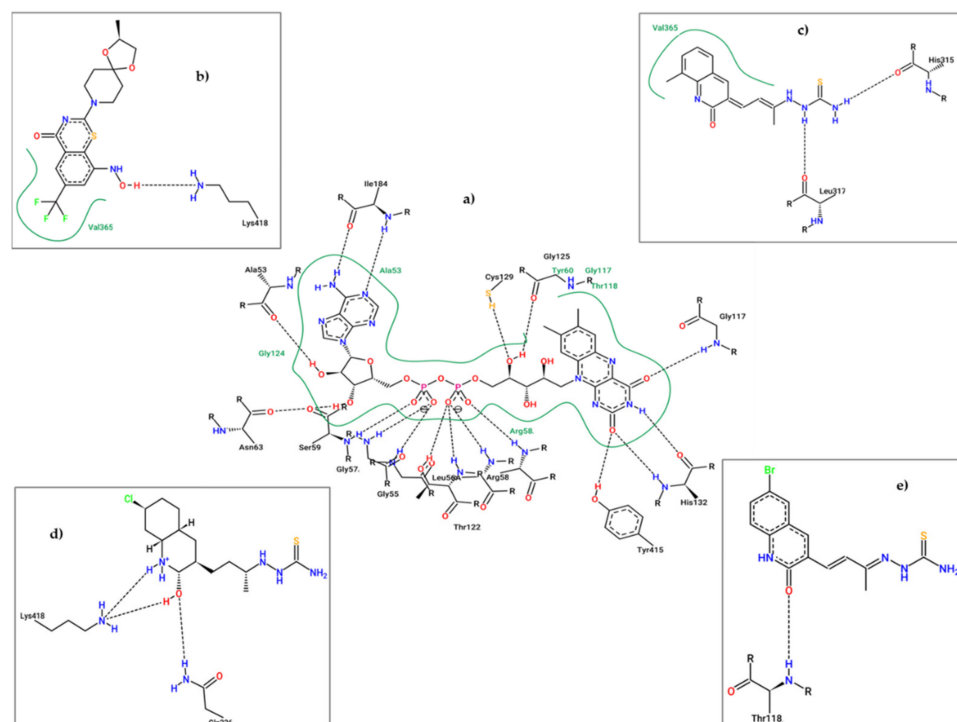


Figure 15. 2D Representation of the interaction between DprE1 and FAD (a), BTZ043 (b), 11c (c), 11d (d), and 11e (e).

The ligand–protein interaction was analyzed using the MMPBSA approach (Kumari et al. 2014). In this method, the free binding energies (ΔG) are computed considering the van der Waals, electrostatic, and solvent-accessible surface area (SASA) energies (Table 6). According to Table 6, all ΔG values were negative, indicating both favorable and stable interaction between the ligand and the receptor; except for **11d**, the more significant contribution to the ΔG were van der Waals interactions, followed by electrostatic energies, suggesting all of the interactions were driven mainly by dipolar interactions. Interestingly, the complex formation for compounds **11d**-enoyl-ACP reductase was mediated by electrostatic contribution (-77 kcal/mol). Finally, according to Table 6, the compounds interacted more significantly with enoyl-ACP reductase than with DprE1. However, the suitable binding energies (from -12.7 to 71.3 kcal/mol) motivated the synthesis and evaluation of all the designed compounds. The difference in binding energy values obtained for both proteins suggests selectivity in molecular recognition; thus, the compounds designed in this work would have more affinity for the InhA protein than DprE1. On the other hand, although these results are not absolutely indicative of a possible mechanism of action, they do provide additional support for their synthesis and subsequent *in vitro* testing.

Table 6. Free binding energy of the interaction in the complex between studied ligands and enzymes.

Enzyme	Compound	van der Waals (kcal/mol)	Electrostatic (kcal/mol)	SASA (kcal/mol)	Binding Energy (kcal/mol)
InhA	11c	-38.20	-7.40	-4.30	-19.30
	11d	-36.60	-77.20	-4.60	-71.30
	11e	-45.00	-7.30	-4.20	-22.90
DprE1	11c	-40.00	-14.20	-4.00	-13.60
	11d	-46.70	-19.60	-4.60	-12.70
	11e	-38.20	-13.10	-3.90	-14.80

2.8. Chemistry

To experimentally validate the results obtained from the computational design, many authors proceed to perform the synthesis of five structures or less [70–73]. Therefore, Table 7 shows the route employed to prepare the designed compounds using the QSAR procedure, supported by docking and dynamic molecular results. The 3-formyl-2-oxo-quinoline precursors **15a–e** were synthesized as presented in Table 7, following the directions of the reported procedures [74]. Two transformations prepared the quinolinone-thiosemicarbazone hybrids **11a–e**. The first consisted in the preparation of the chalcone analog derivatives **16a–e** by a Claisen–Schmidt condensation between the respective 3-formyl-2-oxo-quinoline **15a–e** and an excess of acetone in the presence of 20% NaOH [75]. The mixture was stirred at room temperature for 15 min until all the aldehyde **15** was consumed (monitored by TLC). Then, the reaction mixture was neutralized with AcOH and the precipitate formed was filtered off and washed with a mixture of water/methanol, giving the appropriate chalcone analog derivative **16a–e** in 65–88% yields.

Table 7. General approach for the preparation of the target quinolinone-thiosemicarbazone hybrids **11a–e**.

Compound	R	Yield	Time (h)
11a	H	80	6
11b	6-CH ₃	70	6
11c	8-CH ₃	75	6
11d	7-Cl	85	8
11e	6-Br	85	8

The second transformation consisted of preparing thiosemicarbazones **11a–e** following the general synthetic procedure (Table 7), where the chalcone analog **16** and thiosemicarbazide in EtOH with the addition of AcOH as the catalyst were heated at 80 °C. The synthesized compounds **11a–e** afforded yields ranging from 80 to 92%. The structures of the quinolinone-thiosemicarbazone hybrids **11a–e** were characterized by IR, NMR (in DMSO-*d*₆), and mass spectrometric analysis.

2.9. Antimycobacterial Activity

All the newly synthesized compounds were tested against two different acid-fast slow-growing mycobacteria, *M. tuberculosis* H37Rv and *M. bovis* BCG. Isoniazid was used as a reference control, and results were expressed as minimum inhibitory concentration values (MICs, μM) and are presented in Table 8. Antimycobacterial screening showed that all compounds exhibited potent activity against *Mycobacterium* with MIC values in the range 0.03–0.33 μM against *M. bovis* BCG and 0.13–0.17 μM against *M. tuberculosis* H37Rv. All synthesized compounds showed better MIC values than the reference drug isoniazid (MIC = 0.36 μM). Here, we demonstrated the predictive capacity of the QSAR model against the *M. tuberculosis* H37Rv strain. Compounds with highest activity against *M. bovis* BCG were **11d**, with MIC = 0.03 μM, and **11e** with MIC = 0.13 μM (Table 8). Compounds **11a**

and **11b** presented an excellent inhibition with MIC = 0.17 and 0.16 μM , respectively; the least active derivative was **11c** with MIC = 0.33 μM . The most active compounds against *M. tuberculosis* H37Rv were **11d–e**, with MIC = 0.15 μM and MIC = 0.13 μM , respectively; conversely, the least active compounds were **11a** MIC = 0.17 μM and **11b–c** MIC = 0.16 μM .

Table 8. Antimycobacterial activity against *M. tuberculosis* H37Rv and *M. bovis*.

Compound	<i>M. bovis</i> BCG	<i>M. tuberculosis</i> H37Rv
MICs in μM		
11a	0.17	0.17
11b	0.16	0.16
11c	0.33	0.16
11d	0.03	0.15
11e	0.13	0.13
Isoniazid	0.36	0.36

It is important to note that the experimental values shown in Table 8 (*M. tuberculosis* H37Rv) are in line with the values predicted by model 3, with compounds **11d** and **11e** being the most active. The excellent biological activity of the synthesized compounds is attributed to the incorporation of the thiosemicarbazone system in the quinolinone, since it generates an increase in the molecular volume (parameter **24a**, see Table 4), specifically due to the free rotation of the NH_2 group (due to its sp^3 hybridization). Added to the above, N and S atoms provide a decrease in molecular electronegativity (χ), which could cause the narrow MIC value among the synthesized products (similar values for each product, see Table 4). These latter results support the hypothesis that the distribution of HOMO in the thiosemicarbazone part seems to be a structural factor related to the antimycobacterial activity.

Complementing this work, the antimycobacterium biological activity for compounds **11a** to **11e** was tested against four genetically different lineages of *M. tuberculosis* multiresistant to isoniazid and rifampicin: a *M. tuberculosis* orphan strain with no match in spolDB4 [76]; *M. tuberculosis* Beijing, an emerging pathogen in several areas and a predominant endemic strain in others that is frequently associated with drug resistance [77]; *M. tuberculosis* LAM 9, a predominant genotypic family belonging to the Latin American and Mediterranean (LAM) lineage [78]; and *M. tuberculosis* Haarlem, whose genotype is ubiquitous worldwide and represents about 25% of the isolates in Europe, Central America, and the Caribbean, suggesting a link with the post-Columbus European colonization [79]. Haarlem strains are actively transmitted in urban settings in Colombia [79]. Additionally, two reference strains, *M. tuberculosis* rifampicin resistance strain ATCC 35838 and *M. tuberculosis* isoniazid resistance strain ATCC 35822, were used as internal quality control (Table 9).

Table 9. Antimycobacterial activity against *M. tuberculosis*.

Comp.	<i>M. tuberculosis</i> Orphan	<i>M. tuberculosis</i> Beijing	<i>M. tuberculosis</i> LAM 9	<i>M. tuberculosis</i> Haarlem	<i>M. tuberculosis</i> ATCC 35838	<i>M. tuberculosis</i> ATCC 35822
MICs in μM						
11a	3.49	1.75	0.35	17.46	3.49	3.49
11b	33.29	1.66	16.65	3.33	3.33	3.33
11c	66.58	0.33	3.29	33.29	1.66	0.33
11d	6.23	0.33	3.12	1.56	3.33	6.23
11e	27.38	0.27	2.74	27.37	2.73	1.37
Oxafloxacin	2.67	2.76	2.76	2.76	2.76	2.76

All compounds exhibited activity in the qualitative range of good to excellent against the different families of multiresistant *M. tuberculosis*, with MIC values in the range 0.27–66.58 μM (Table 9). Interestingly, many of these compounds showed better activity than the standard drugs (Oxofloxacin, MIC = 2.76 μM). Furthermore, results in Table 9 show that *M. tuberculosis Beijing* was the most susceptible to compounds developed in this work, with MIC values of 0.27–1.75 μM . Noteworthy, compounds **11c–e** showed the best activity against most of the tested *M. tuberculosis* multiresistant strains. Compound **11e**, having a bromine substituent on the quinolinone ring, showed the highest activity against *M. tuberculosis Beijing*, being tenfold more potent than Oxofloxacin. On the other hand, compound **11c**, with a methyl group at the 8 position on the quinolinone ring, showed excellent activity against *M. tuberculosis Beijing* and *M. tuberculosis ATCC 35822*. Similarly, compounds **11d** (with chlorine substituent at the 6 position) displayed good growth inhibition against the *M. tuberculosis Beijing* and *M. tuberculosis Haarlem* strain, with MIC values of 0.33 μM and 1.56 μM , respectively.

2.10. Cytotoxicity

The cytotoxic activity of compounds **11a–e** was determined by an MTT assay on Vero cells (ATCC[®] CCL-81TM) with NaDS as a positive control and dimethylsulfoxide (DMSO) as a negative control. The growth of the Vero cell line was expressed as half maximal inhibitory concentration values (IC₅₀). Therefore, the selectivity index (SI) was calculated as the ratio between IC₅₀ in Vero cells to the concentration that can kill the mycobacteria. The results are summarized in Table 10, revealing that compounds **11a–e** were highly cytotoxic with IC₅₀ values in the range of 1.91–3.53 μM . Compounds **11b** and **11e** presented minor toxicity. However, many of these compounds showed a selectivity index of >10 against *M. bovis* BCG and *M. tuberculosis* H37Rv strains, **11b** and **11e** being the most potent, indicating that these compounds selectively inhibit *M. tuberculosis* more than normal cells.

Table 10. Cytotoxic activity (IC₅₀) in Vero cells and selectivity index (SI) of the active synthetic hybrids **11a–e** strains of *M. tuberculosis*.

Compound	Cytotoxicity IC ₅₀ -Vero Cells μM	a	b	c	d	e	f	g	h
11a	1.91	11.24	11.24	0.55	1.09	5.46	0.11	0.55	0.55
11b	3.53	22.06	22.06	0.11	2.13	0.21	1.06	1.06	1.06
11c	1.90	5.75	11.88	0.03	5.76	0.58	0.06	1.14	5.76
11d	1.65	55.00	11.00	0.26	5.00	0.53	1.06	0.50	0.26
11e	2.20	16.92	16.92	0.08	8.15	0.80	0.08	0.81	1.61

(a) *M. bovis* BCG; (b) *M. tuberculosis* H37Rv; (c) *M. tuberculosis orphan*; (d) *M. tuberculosis Beijing*; (e) *M. tuberculosis* LAM 9 (sit 42); (f) *M. tuberculosis Haarlem*; (g) *M. tuberculosis* ATCC 35838 RR; (h) *M. tuberculosis* ATCC 35822 RI.

In summary, the results obtained in this work suggest that the combination of QSAR and molecular dynamics guided the synthesis of the different compounds with anti-TB activity; moreover, in some compounds, the bioactivity against other strains was more significant than that of the standard compounds. Finally, all the compounds developed in this work showed a selectivity index against *M. tuberculosis* H37Rv >10, with compound **11e** showing the best performance.

3. Materials and Methods

3.1. Data Collection

The selection criteria were based on compounds bearing quinoline and/or thiosemicarbazone moiety in their structures; furthermore, the guidelines recommended by Alexander Tropsha for the construction of the virtual library were followed [80–83]. In addition, we calculated the minimum inhibitory concentration of the biological activity using the

same protocol. In this work, quinolines are the central nucleus; therefore, a search for antituberculosis quinolines compounds was performed using databases such as SciFinder and PubChem. Subsequently, we searched for thiocarbamides with biological activity against tuberculosis. However, we encountered two obstacles: most of the thiocarbamides were coupled to nuclei other than quinolines outside the application domain. Some thiocarbamides were reported using antituberculosis activities measured in other than IC_{50} or mg/mL .

Under the criteria explained above, 32 compounds, including three coupled thiocarbamides and quinolines, met the selection criteria. Thirty-two compounds were selected from the bibliography [84–88] and their structures are shown in Figure 16.

It is important to note that the mechanism of action of the selected structures was not taken into account for the construction of the data, since it is not a requirement for the elaboration of QSAR models according to the different research related to this methodology [13,89–96]. Nevertheless, the structural diversity of the compounds studied here, with molecular structures similar to compounds already reported as antituberculosis (fluoroquinolones and quinolones), in addition to the great diversity of isosteric substituents on the pharmacophoric nuclei, guarantee a domain of application suitable for the rational design of new drugs.

3.2. Minimum Energy Structures and Molecular Descriptors Calculation

The structures were drawn using Avogadro software (Figure 16) [97], and a minimum energy conformer research was applied. After finding the minimum energy conformers for each structure, these were changed to gif format and optimized at B3LYP/6–31(d,p) theory level employing Gaussian for Linux [98]. The minimum energy structures were confirmed using frequency calculation. The combination of density functional theory with the set base 6–31G(d,p) was supported by its extraordinary capacity to reproduce experimental results in molecular reaction parameters and QSAR approximations [99–104].

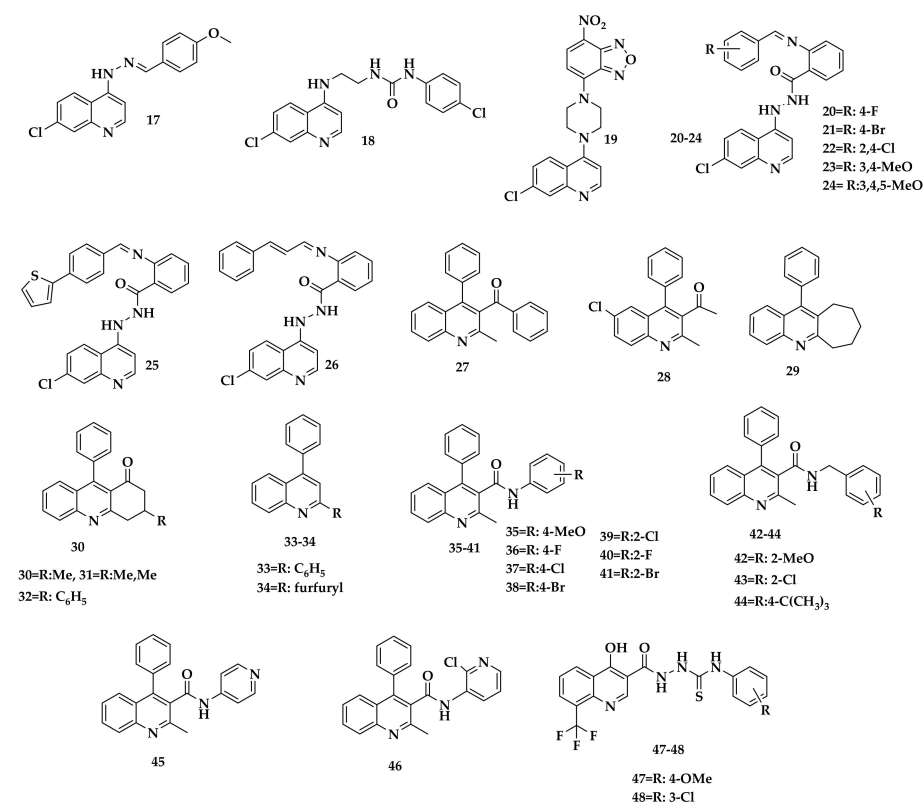


Figure 16. Chemical structures of quinoline-based compounds studied in this work.

3.3. Descriptor Calculations

Once the minimum energy structures were assured, three molecular descriptors were computed for the entire data: electronic [105], thermodynamics [106], and topographic [107]. First, electronic descriptors were calculated using conceptual density functional theory [108].

All the electronic molecular descriptors were based on frontier molecular orbitals taken from the output of the optimized structure. Hence, HOMO (highest occupied molecule orbital) and LUMO (lowest unoccupied molecular orbital), were used to calculate other electronic descriptors such as molecular ionization potential (IP), electronic affinity (EA), electronegativity (χ), electronic potential (μe), electrophilic index (ω), molecular hardness (η), molecular softness (s), using the following Equations:

$$(\chi) = \frac{1}{2}(PI + AE) \quad (4)$$

$$(\mu e) = -\chi = -\frac{PI + EA}{2} \quad (5)$$

$$(\omega) = \frac{(\mu e)^2}{2n} \quad (6)$$

$$(\eta) = \frac{1}{2}(PI - AE) \quad (7)$$

$$(S) = \frac{1}{2n} \quad (8)$$

IP and EA are ionization potential and electronic affinity, respectively; in both cases, parameters were calculated by assuming that the electronic geometry of the cation or anion remained equal to that of the neutral species [109]. Thus, both were calculated employing Equations (9) and (10).

$$EA = E^- - E^0 \quad (9)$$

$$IP = E^+ - E^0 \quad (10)$$

Thermodynamics descriptors are those related to Gibbs equations: molar refractivity [109], enthalpy (H), entropy (S), Gibbs energy (G), and molar heat capacity; all of them were calculated for the entire data at 25 °C employing the frequency calculation outputs. On the other hand, the topological molecular descriptors such as accessible area, molecular area, solvent excluded volume, H acceptor atoms, H donor atoms, ovality, partition coefficient, Balaban index, cluster counter, molecular topological index, rotatable number of atoms, polar surface area, radius, attribute form, coefficient form, the sum of degrees, sum of degrees of valence, topological diameter, total connectivity, total connectivity of valence, and Wiener index were calculated employing Chembiooffice 18.1 software [109]. Finally, topographic 3D molecular descriptors suggested for cheminformatics studies such as QSAR were calculated using QuBiLS-MIDAS [110]. A total of 3031 3D molecular descriptors were estimated based on many algebraic operations considering linear, bilinear, and quadratic indexes for all molecules in the dataset [110].

3.4. QSAR Models

The computed molecular descriptors for the entire data were tabulated and used as the independent variable; the anti-TB activity was used as a dependent variable ($pMIC = -\log(1/MIC)$), where experimental MIC (MIC_{exp}) represent the minimum inhibitory concentration (in mol/L). A multiple regression analysis (MRA) was performed using the IBM SPSS Statistics 25 software for Windows to find the most molecular descriptors correlated with the biological activity. Different variable selection methods were used for introduction, stepwise, elimination, backward, and forward selection [110].

In all cases, the obtained models were considered “meaningful” by analyzing the statistic quality; statistical parameters such as the regression coefficient (R), the Fisher

value (F), and the standard deviation (s) were computed; as already known, the higher the r^2 values, the better the model. In the same line, F values correlated variance (r^2) by the number of degrees of freedom with the unexplained variance ($1 - r^2$) by the number of variables in the model. Thus, the higher the percentage of variance explained by the model, the higher the F and, consequently, the better the model. A Pearson correlation was employed to investigate any correlated molecular descriptors in the models. A Pearson's coefficient higher than 0.7 was considered a "strong association" between two independent variables; consequently, one of the correlated independent variables was ruled out.

3.5. Applicability Domain (AD)

For the QSAR building and validation, the applicability domain analysis is a fundamental requirement for determining the model's reliability and discarding any incorrect dependent variable. It can be defined as the theoretical spatial section limited by the structure, biological activity, and the descriptors selected in the regression model [42,111]. The AD analysis was carried out using a William plot procedure [112].

3.6. Validation Procedures

The robustness of the generated models was examined by employing several statistical validation procedures such as the leave-one-out cross-validation and leave-many-out cross-validation methods (Q_{LOO} and Q_{LMO}); for the external validation bootstrapping [113] and y-scrambling [114] were employed. Finally, the Tropsha test criterium was applied to the best models [115].

3.7. Molecular Docking

Molecular docking is a versatile tool that allows finding minimum energies of protein–ligand interaction structures [116] and has been used as a standard tool for designing and synthesizing new potential anti-TB compounds [69,89,117–121].

This work used molecular docking to test the *in silico* anti-TB activity of new structures designed by analyzing QSAR models. Two protein targets were used for this goal: enoyl-acyl carrier protein reductase (InhA) and decaprenylphosphoryl- β -D-ribose-2'-oxidase (DprE1). The InhA is an enzyme involved in the biosynthesis of mycolic acid, the major *Mycobacterium* cell wall component [122]; moreover, this is the target of the anti-TB first-line compound isoniazid [123]. On the other hand, decaprenylphosphoryl- β -d-ribose 2'-epimerase (DprE1) is an essential enzyme involved in the formation of lipoarabinomannan arabinogalactan compounds, which are critical to cellular wall synthesis [124]. After selecting the targets, the structures of the proteins were retrieved from the protein data bank webpage (<https://www.rcsb.org/> accessed on 1 December 2022) as follows: InhA, PDB ID: 2PR2 and DPrE1, PDB ID: 6HFW. Likewise, their inhibitors, such as (4S)-isonicotinic-acetyl-nicotinamide-adenine dinucleotide (INH-NADP complex) and 8-(oxidanyl-amino)-2-piperidin-1-yl-6-(trifluoromethyl)-1,3-benzothiazin-4-one respectively, were retrieved from the PubChem webpage (<https://pubchem.ncbi.nlm.nih.gov/> 1 December 2022) and optimized at B3LYP/6-31(d,p) level of theory.

The structure of proteins with their inhibitors was cleaned by withdrawing any water, inhibitor, and non-native ligands molecules. Then, the proteins cleaned were redocked against their inhibitors to ensure that the docking protocols' output showed similarities to the protein retrieved from the PDB web page. For this aim, the autodock vina tool was used [125]. The proteins' PDB ID, active sites, and inhibitors used in the redocking protocols and grillaBox sizes are shown in Table 11.

Table 11. Docking information.

Protein	PDB:ID	Active Site (x, y, z)	Inhibitor	Grilla Box Size (x, y, z)
DprE1	6HFW	13.869, −21.448, 37.131	8-(oxidanylamino)-2-piperidin-1-yl-6-(trifluoromethyl)-1,3-benzothiazin-4-one (BTZ043)	22, 22, 22
InhA	2PR2	−1.702, −27.226, 15.656	INH-NADP	22, 22, 22

3.8. Molecular Dynamics

Molecular dynamic simulations were carried out to evaluate the different ligand–receptor complexes' stability over time and to obtain insights into the interactions formed. For the calculation, two enzymes were chosen, decaprenylphosphoryl- β -D-ribose 2'-epimerase and enoyl-acyl reductase, while the ligands **11c**, **46d**, and **46e** were used. Furthermore, the most favorable conformation of the ligands in the enzymes resulting from docking calculation was chosen as input for the molecular dynamics simulation. For all the calculations, Gromacs 2019 [126] was employed, AMBER99SB-ILDN [127] force field implemented in Gromacs 2019 was picked to build the topology of the enzymes.

On the other hand, the topology was built using the ACPYPE server [126] and the generalized AMBER force field (GAFF) for the ligands. Before the simulation, the enzyme–ligand complexes were solvated using a three-point water model (TIP3) employing a cube shape and neutralized using chlorine or sodium atoms. Then, the complex was relaxed and equilibrated using constant NVT (number of particles, volume, temperature) and NPT (number of particles, pressure, and temperature) protocols for 100 ps at 300 K [128]. Once the system was equilibrated, the 200 ns simulation was carried out, setting the temperature at 300 K and the pressure to 1 bar [128].

3.9. Molecular Orbitals

In the past twenty years, frontier orbitals have played a pivotal role in understanding the molecular interaction between ligand–receptor and a specific biological activity [129–137]. Typically, the shape and electron density of boundary orbitals indicate the most reactive regions of a molecule. However, in other cases, compounds with the same biological activity follow a similar pattern of boundary orbitals [48]. The frontier molecular orbitals for the design structures were retrieved from the optimized output using the B3LYP/6-31G(d,p) level of theory; the isosurfaces were generated using 0.02 eV isovalues.

3.10. Chemistry

Reagents and solvents were purchased from Sigma (St. Louis, MO, USA) and Merck (Darmstadt, Germany). Melting points were measured using a Stuart SMP3 melting point apparatus. IR spectra were recorded on a Shimadzu FTIR 8400 ATR spectrophotometer. Mass spectra were run on a SHIMADZU-GCMS 2010-DI-2010 spectrometer (equipped with a direct inlet probe) operating at 70 eV. In addition, ^1H and ^{13}C NMR spectra were recorded on a Bruker Avance 400 spectrophotometer operating at 400 MHz and 100 MHz, respectively, using DMSO- d_6 as solvent and tetramethylsilane as the internal standard. TLC analyses were performed on 0.2 mm pre-coated aluminum plates of silica gel 60 F₂₅₄ (Merck, Darmstadt, Germany) and spots visualized were with ultraviolet irradiation.

General procedure for the synthesis of the (E)-3-(3-oxobut-1-en-1-yl)quinolin-2(1H)-ones 16a–e. A mixture of acetone (10 mL, 136 mmol), the corresponding 3-formyl-2-oxoquinoline precursors **15a–e** (1.0 mmol) and 20% aq NaOH (5 mL) was stirred at room temperature for 15 min and the evolution of the reaction was checked by TLC. Once the reaction was complete, the resulting precipitate was collected by filtration under vacuum

and washed several times with water and ethanol to afford **16a–e**. No further purification was required.

General procedure for the synthesis of the novel quinolinone-based thiosemicarbazones 11a–e. A mixture of (*E*)-3-(3-oxobut-1-en-1-yl)quinolin-2(1H)-one **16a–e** (1 mmol), thiosemicarbazide (1.5 mmol), and acetic acid (50 μ L) in EtOH (10 mL) was heated at reflux for 6–8 h. The precipitate thus produced was filtered and washed several times from EtOH to give products **11a–e**. No further purification was required.

(*E*)-2-((*E*)-4-(6-Methyl-2-oxo-1,2-dihydroquinolin-3-yl)but-3-en-2-ylidene)hydrazine-1-carbothioamide 11a. Yellow solid. 80% yield; mp = 240 °C. FTIR (ATR) ν (cm^{-1}): 3404 (NH), 3095 (NH), 1600 (C=O). ^1H NMR (400 MHz, DMSO- d_6) δ 2.12 (s, 3H, CH₃), 7.10 (d, J = 16.5 Hz, 1H, =CH), 7.14 (m, 1H), 7.28 (d, J = 8.2 Hz, 1H), 7.42 (d, J = 16.5 Hz, 1H, =CH), 7.5 (m, 1H), 7.67 (d, 1H), 7.8 (s, 1H, NH₂), 8.15 (s, 1H), 8.30 (s, 1H, NH₂), 10.30 (s, 1H, NH), 12.90 (s, 1H, NH). ^{13}C NMR (101 MHz, DMSO- d_6) δ 12.4 (CH₃), 115.3, 119.8 (Cq), 122.6, 127.9, 128.5, 129.1, 130.9 (Cq), 137.1, 138.5, 149.5 (Cq), 161.2 (C=O), 179.1 (Cq). EI MS (70 eV): m/z (%): 286 (M⁺, 10), 170 (100), 115 (61), 211 (42), 140 (40), 60 (41), 226 (38), 89 (36), 152 (30), 269 (27), 197 (22), 244 (21).

(*E*)-2-((*E*)-4-(6-Methyl-2-oxo-1,2-dihydroquinolin-3-yl)but-3-en-2-ylidene)hydrazine-1-carbothioamide 11b. Yellow solid. 70% yield; m.p = 251 °C. FTIR (ATR) ν (cm^{-1}): 3415 (NH), 3245 (NH), 3155 (NH), 1599 (C=O). ^1H NMR (400 MHz, DMSO- d_6) δ 2.14 (s, 3H, CH₃), 2.35 (s, 3H, CH₃), 7.13 (d, J = 16.5 Hz, 1H, =CH), 7.22 (d, J = 8.3 Hz, 1H), 7.33 (d, J = 9.8 Hz, 1H), 7.49–7.42 (m, 2H), 7.8 (s, 1H, NH), 8.08 (s, 1H), 8.28 (s, 1H, NH), 10.28 (s, 1H, NH), 11.90 (s, 1H, NH). ^{13}C NMR (101 MHz, DMSO- d_6) δ 12.4 (CH₃), 20.9 (CH₃), 115.2, 119.8 (Cq), 127.8, 127.9, 129.4, 131.5 (Cq), 132.1, 132.3, 136.5 (Cq), 137.0, 149.7 (Cq), 161.2 (C=O), 179.2 (Cq). EI MS (70 eV): m/z (%): 300 (M⁺, 7), 184 (100), 60 (67), 42 (44), 225 (39), 40 (38), 283 (37), 128 (37), 154 (36), 77 (33), 240 (32), 115 (31), 211 (22), 167 (19), 258 (15), 102 (15).

(*E*)-2-((*E*)-4-(8-Methyl-2-oxo-1,2-dihydroquinolin-3-yl)but-3-en-2-ylidene)hydrazine-1-carbothioamide 11c. Yellow solid. 75% yield; mp = 241 °C. FTIR (ATR) ν (cm^{-1}): 3413 (NH), 3228 (NH), 3149 (NH), 1581 (C=O). ^1H NMR (400 MHz, DMSO- d_6) δ , 2.16 (s, 3H, CH₃). 2.45 (s, 3H, CH₃), 7.19–7.08 (m, 2H), 7.35 (d, J = 7.2 Hz, 1H), 7.43 (d, J = 16.6 Hz, 1H, =CH), 7.53 (d, J = 7.8 Hz, 1H), 7.83 (s, 1H, NH), 8.17 (s, 1H), 8.29 (s, 1H, NH), 10.30 (s, 1H, NH), 11.08 (s, 1H, NH). ^{13}C NMR (101 MHz, DMSO- d_6) δ 12.4 (CH₃), 17.6 (CH₃), 119.9 (Cq), 122.4, 123.7 (Cq), 126.7, 127.6 (Cq), 128.9, 132.1, 132.6 (Cq), 136.9 (Cq), 137.6, 149.6 (C=O, Cq), 161.8 (C=O, Cq), 179.22 (Cq). EI MS (70 eV): m/z (%): 300.05 (M⁺, 13), 184 (100), 60 (53), 240 (45), 225 (41), 154 (32), 283 (32), 128 (30), 141 (27), 115 (26), 258 (26), 77 (26), 211 (24), 167 (18), 102 (13).

(*E*)-2-((*E*)-4-(7-Chloro-2-oxo-1,2-dihydroquinolin-3-yl)but-3-en-2-ylidene)hydrazine-1-carbothioamide 11d. Yellow solid. 85 % yield; mp = 246 °C. FTIR (ATR) ν (cm^{-1}): 3465 (NH), 3320 (NH), 3162 (NH), 1594 (C=O). ^1H NMR (400 MHz, DMSO- d_6) δ 2.14 (s, 3H, CH₃), 7.10 (d, J = 16.6 Hz, 1H, =CH), 7.24 (dd J = 8.4 Hz, 1H), 7.33 (s, 1H), 7.44 (d, J = 16.5 Hz, 1H, =CH), 7.70 (dd, 1H), 7.80 (s, 1H, NH), 8.17 (s, 1H), 8.29 (s, 1H, NH), 10.31 (s, 1H, NH), 12.05 (s, 1H, NH). ^{13}C NMR (101 MHz, DMSO- d_6) δ 12.4 (CH₃), 114.6, 118.6 (Cq), 122.8, 128.3, 128.8 (Cq), 130.3, 132.7, 135.2 (Cq), 136.4, 139.2 (Cq), 149.4 (Cq), 161.2 (C=O), 179.2 (Cq). EI MS (70 eV): m/z (%): 320.05 (M⁺, 2), 303 (74), 204 (100), 140 (76), 77 (77), 140 (75), 303 (72), 71 (64), 69 (68), 97 (55), 43 (54), 261 (49), 57 (47), 94 (48), 245 (44), 113 (43), 151 (41), 208 (39), 305 (29), 313 (25), 263 (25), 167 (20), 230 (20), 186 (15), 288 (14).

(*E*)-2-((*E*)-4-(6-Bromo-2-oxo-1,2-dihydroquinolin-3-yl)but-3-en-2-ylidene)hydrazine-1-carbothioamide 11e. Yellow solid. 85% yield; mp = 253 °C. FTIR (ATR) ν (cm^{-1}): 3412 (NH), 3267 (NH), 3162 (NH), 1646 (C=O). ^1H NMR (400 MHz, DMSO- d_6) δ 2.14 (s, 3H, CH₃), 7.10 (d, J = 16.5 Hz, 1H, =CH), 7.25 (d, J = 8.7 Hz, 1H), 7.44 (d, J = 16.6, 1.8 Hz, 1H, =CH), 7.62 (d,d, J = 8.7, 2.1 Hz, 1H), 7.81 (s, 1H, NH₂), 7.89 (d, J = 1.8 Hz, 2H), 8.11 (s, 1H), 8.30 (s, 1H, NH), 10.31 (s, 1H, NH), 12.09 (s, 1H, NH). ^{13}C NMR (101 MHz, DMSO- d_6) δ 12.4. (CH₃), 114.1 (Cq), 117.4, 121.5 (Cq), 128.7, 129.1 (Cq), 130.2, 133.0, 133.3, 135.7, 137.4 (Cq), 149.4 (Cq), 161.1 (Cq), 179.2 (Cq). EI MS (70 eV): m/z (%): 140 (100), 365.85 (M⁺, 2), 247

(81), 249 (80), 114 (61), 289 (50), 143 (52), 348 (45), 346 (43), 169 (35), 304 (33), 36 (34), 42 (34), 274 (32), 89 (22), 276 (22), 99 (17), 151 (18), 210 (12), 319 (10).

3.11. Antimycobacterial Activity

Antimicrobial activity, was measured by spot culture growth inhibition assay (SPOTi) [138]. In order to evaluate the minimum inhibitory concentration (MIC) values for the different synthetic compounds **11**, these were tested against the laboratory strains: *M. tuberculosis* H37Rv, *M. tuberculosis* lineage orphan, *M. tuberculosis* lineage Beijing, *M. tuberculosis* lineage LAM 9, *M. tuberculosis* lineage Haarlem, *M. tuberculosis* ATCC 35838 (rifampicin resistant) and *M. tuberculosis* ATCC 35822 (isoniazid resistant). Biological activity was tested in a level 3 biosafety laboratory of the Colombian National Health Institute. *M. bovis* assays were performed at Universidad del Norte at the biological and chemical research laboratory. Briefly, the compound was dissolved in dimethylsulfoxide (DMSO) in a 200 mg/mL stock solution; from this, a serial dilution was made in a sterile 24-well microplate, allowing for evaluation concentrations of 100–0.01 mg/L. First, 2.0 µL of the dilutions were dispensed in each dish. Next, 2.0 mL of Middlebrook 7H10 medium was added appropriately and supplemented with glycerol and OADC (oleic acid, albumin, dextrose, and catalase). The medium was allowed to cool, and then in the middle of each well 2.0 µL of a dilution of the inoculum (containing about 10⁶ CFU/mL) of *M. tuberculosis* H37Rv or *M. bovis* BCG was added. The isoniazid drug was used as a positive standard. The plates were covered for 2–3 weeks at 37 °C. After the incubation period, the plates were observed and the MIC was determined as the minimum concentration on which growth was not observed. The experiment was repeated on a different day observing exactly the same results.

3.12. Cytotoxicity Assay

Vero cells (ATCC[®] CCL-81[™]), were cultured in Dulbecco Modified Eagle Medium (DMEM) supplemented with 10% bovine fetal serum and 1% streptomycin–penicillin and passaged twice before the assay in 21 cm² cell culture Petri dishes at 37 °C in 5% CO₂ incubator and 100% humidity. Cells were then cultured in 96-well plates for 24 h before the assay to a cell density of 104 cells per well. A 96-well master plate was used to dilute of the compounds in DMEM medium, by diluting 5 mL of the 100 mg/mL DMSO stock of the compounds into 195 mL of the DMEM medium and performing twofold serial dilution with 100 mL. One hundred microliters of this solution was transferred to each plate containing the Vero cells and incubated for 48 h. Five percent NaDS was used as a positive control and DMSO as negative control under the same dilution conditions. Ten milliliters of a freshly prepared MTT (3-(4,5-dimethyl-2-thiazolyl)-2,5-diphenyl-2H-tetrazoliumbromide) solution in PBS at 5 mg/mL was added to each well, and the plates were further incubated for 1.5 h. The media was then removed and 130 µL of DMSO was added to each well. After 30 min of incubation, the absorbance was read at 530 nm on a microplate reader. The experiment was performed in duplicate on different days with different cell cultures and different stock of the compounds. The IC₅₀ (in µM) values were determined by interpolation from the mean absorbance data of 100% viability (negative control) and 0% viability (positive control).

4. Conclusions

Thirty-two compounds with anti-TB activity against the *M. tuberculosis* H37RV strain were retrieved from the literature to obtain possible quantitative structure–anti-TB activity correlations. These compounds were optimized at the B3LYP/6-31G (d,p) level of theory; the minimum energy structures were used to calculate electronic, thermodynamic, and topographical molecular descriptors. As a result, model 3 was chosen according to statistics and the lowest number of attributes, so it was used as a guiding model for generating new compounds. The van der Waals volume, electron density, and electronegativity model results suggest a pivotal role in anti-TB activity; as such, van der Waals volume increases biological activity and electron density and the electronegativity decrease the anti-TB

activity. Five new compounds were designed by taking compound 26 as a base structure and adding substituents according to model 3. The designed compounds were compared electronically with reported anti-TB compounds, such as BTZ043 and isoniazid. It was found that compounds with frontier orbitals distributed on opposite sides of the molecules exhibited higher activity values than those without this behavior. In addition, docked compounds against enoyl-acyl carrier protein reductase (InhA) and decaprenylphosphoryl- β -D-ribose-2'-oxidase (DprE1) showed affinity values ranging from -8.5 to -7.1 Kcal/mol; compounds **11d** and **11e** showed the best behavior towards both molecular targets. Protein–compound molecular dynamics calculations resulted in negative binding energy in the range of -71.3 to -12.7 kcal/mol. In all cases, the compounds bound to each target at the catalytic site reported in the literature, which means that there is a high probability that they were inhibitors of these two proteins. The newly designed compounds were synthesized and evaluated for their anti-TB activity against *M. bovis* BCG, *M. tuberculosis* H37Rv, and six strains of *M. tuberculosis* resistant to rifampicin and isoniazid. Most compounds showed better MIC values than the reference drugs (isoniazid and oxafloxacin). Compounds **11d** and **11e**, with chlorine and bromine groups on the quinolinone ring, were found to be the most active with MIC values of 0.15 μ M and 0.13 μ M, respectively, against *M. tuberculosis* H37Rv and selectivity index of >10 . This study suggests that **11d** and **11e** possess great potential in developing of new anti-TB drugs and can serve as hits for in vivo studies to validate their potential as lead compounds.

Supplementary Materials: The following are available online at <https://www.mdpi.com/article/10.3390/antibiotics12010061/s1>, Figure S1: (a) Parity diagram MIC exp versus MICp; (b) Parity diagram QLoo vs. MIC exp; (c) graphic residual vs. MIC exp; (d) graphic residual QLoo vs. MIC exp, Figure S2. The frontier orbital for the designed compounds 11a–e from the QSAR model. HOMO: Highest occupied molecular orbital; LUMO: low unoccupied molecular orbital. BTZ: Benzothiazinone derivatives, Figure S3. ^1H and ^{13}C NMR spectrum of **11a**, Figure S4. ^1H , ^{13}C NMR and DEPT 135 NMR spectrum of **11b**, Figure S5. ^1H , ^{13}C NMR and DEPT 135 NMR spectrum of **11c**, Figure S6. ^1H , ^{13}C NMR and DEPT 135 NMR spectrum of **11d**, Figure S7. ^1H , ^{13}C NMR and DEPT 135 NMR spectrum of **11e**, Table S1: Observed and predictive and experimental activities (and their residuals) of the set of quinoline derivatives.

Author Contributions: J.V., investigation; data curation; formal analysis; writing—original draft; J.R.M., S.A.C. and J.L.P., methodology, writing—review and editing; V.R., G.P., L.V., A.B., A.C. and O.V. planned and performed the antimycobacterial assays and review and editing; B.I., R.A., J.Q. and A.I., methodology, writing—review and editing; E.M. and D.I., conceptualization; formal analysis; investigation; resources; data curation; writing—original draft; writing—review and editing; supervision and project administration. All authors approved the final manuscript. All authors have read and agreed to the published version of the manuscript.

Funding: This research received no external funding.

Institutional Review Board Statement: Not applicable.

Informed Consent Statement: Not applicable.

Data Availability Statement: Not applicable.

Acknowledgments: The authors thank Universidad del Norte, Instituto Nacional de Salud, Bogotá 111321, Universidad del Valle and MINCIENCIAS-Project Number: 201477758055 (contract. No. 777 de 2018) for financial support.

Conflicts of Interest: The authors declare no conflict of interest.

References

1. Dagne, B.; Desta, K.; Fekade, R.; Amare, M.; Tadesse, M.; Diriba, G.; Zerihun, B.; Getu, M.; Sinshaw, W.; Seid, G.; et al. The Epidemiology of First and Second-Line Drug-Resistance Mycobacterium Tuberculosis Complex Common Species: Evidence from Selected TB Treatment Initiating Centers in Ethiopia. *PLoS ONE* **2021**, *16*, e0245687. [CrossRef] [PubMed]
2. Visca, D.; Ong, C.W.M.; Tiberi, S.; Centis, R.; D'Ambrosio, L.; Chen, B.; Mueller, J.; Mueller, P.; Duarte, R.; Dalcolmo, M.; et al. Tuberculosis and COVID-19 Interaction: A Review of Biological, Clinical and Public Health Effects. *Pulmonology* **2021**, *27*, 151–165. [CrossRef] [PubMed]
3. Kranzer, K.; Khan, P.; Godfrey-Fausset, P.; Ayles, H.; Lönnroth, K. Tuberculosis Control. *Lancet* **2016**, *387*, 1159–1160. [CrossRef]
4. Shah, M.; Dorman, S.E. Latent Tuberculosis Infection. *N. Engl. J. Med.* **2021**, *385*, 2271–2280. [CrossRef] [PubMed]
5. Natarajan, A.; Beena, P.M.; Devnikar, A.V.; Mali, S. A Systemic Review on Tuberculosis. *Indian J. Tuberc.* **2020**, *67*, 295–311. [CrossRef] [PubMed]
6. The Global Fund to Fight AIDS Global Fund Applauds Japan's Major Commitment to Help End AIDS, Tuberculosis and Malaria and Strengthen Systems for Health. Available online: <https://www.theglobalfund.org/en/news/2022/2022-08-27-global-fund-applauds-japans-major-commitment-to-help-end-aids-tuberculosis-and-malaria-and-strengthen-systems-for-health/> (accessed on 1 September 2022).
7. Lobo, N.; Brooks, N.A.; Zlotta, A.R.; Cirillo, J.D.; Boorjian, S.; Black, P.C.; Meeks, J.J.; Bivalacqua, T.J.; Gontero, P.; Steinberg, G.D.; et al. 100 Years of Bacillus Calmette–Guérin Immunotherapy: From Cattle to COVID-19. *Nat. Rev. Urol.* **2021**, *18*, 611–622. [CrossRef] [PubMed]
8. Iradukunda, A.; Ndayishimiye, G.-P.; Sinarinzi, D.; Odjidja, E.N.; Ntakaburimvo, N.; Nshimirimana, I.; Izere, C. Key Factors Influencing Multidrug-Resistant Tuberculosis in Patients under Anti-Tuberculosis Treatment in Two Centres in Burundi: A Mixed Effect Modelling Study. *BMC Public Health* **2021**, *21*, 2142. [CrossRef]
9. Ali, A.; Ali, A.; Salahuddin; Bakht, M.A.; Ahsan, M.J. Synthesis and Biological Evaluations of *N*-(4-Substituted Phenyl)-7-Hydroxy-4-Methyl-2-Oxoquinoline-1(2*H*)-Carbothioamides. *Polycycl. Aromat. Compd* **2021**, *42*, 4910–4921. [CrossRef]
10. World Health Organization. *Global Tuberculosis Report 2021*; WHO: Geneva, Switzerland, 2021; ISBN 978-92-4-003702-1.
11. Allué-Guardia, A.; García, J.I.; Torrelles, J.B. Evolution of Drug-Resistant Mycobacterium Tuberculosis Strains and Their Adaptation to the Human Lung Environment. *Front. Microbiol.* **2021**, *12*, 612675. [CrossRef]
12. Mase, S.R.; Chorba, T. Treatment of Drug-Resistant Tuberculosis. *Clin. Chest Med.* **2019**, *40*, 775–795. [CrossRef]
13. Adeniji, S.E.; Uba, S.; Uzairu, A. Theoretical Modeling for Predicting the Activities of Some Active Compounds as Potent Inhibitors against Mycobacterium Tuberculosis Using GFA-MLR Approach. *J. King Saud Univ.Sci.* **2018**, *31*, 1151–1166. [CrossRef]
14. Neves, B.J.; Braga, R.C.; Melo-Filho, C.C.; Moreira-Filho, J.T.; Muratov, E.N.; Andrade, C.H. QSAR-Based Virtual Screening: Advances and Applications in Drug Discovery. *Front. Pharmacol.* **2018**, *9*, 1275. [CrossRef] [PubMed]
15. Braga, R.; Alves, V.; Silva, A.; Nascimento, M.; Silva, F.; Liao, L.; Andrade, C. Virtual Screening Strategies in Medicinal Chemistry: The State of the Art and Current Challenges. *Curr. Top. Med. Chem.* **2014**, *14*, 1899–1912. [CrossRef] [PubMed]
16. Martins, F.; Santos, S.; Ventura, C.; Elvas-Leitão, R.; Santos, L.; Vitorino, S.; Reis, M.; Miranda, V.; Correia, H.F.; Aires-de-Sousa, J.; et al. Design, Synthesis and Biological Evaluation of Novel Isoniazid Derivatives with Potent Antitubercular Activity. *Eur. J. Med. Chem.* **2014**, *81*, 119–138. [CrossRef] [PubMed]
17. Melo-Filho, C.C.; Braga, R.C.; Andrade, C.H. 3D-QSAR Approaches in Drug Design: Perspectives to Generate Reliable CoMFA Models. *Curr. Comput. Aided Drug Des.* **2014**, *10*, 148–159. [CrossRef] [PubMed]
18. Hadni, H.; Mazigh, M.; El Hallaoui, M. QSAR and Molecular Docking Studies of 4-Anilinoquinoline-Triazine Hybrids as Pf-DHFR Inhibitors. *Mediterr. J. Chem.* **2019**, *8*, 84–93. [CrossRef]
19. Patel, S.R.; Gangwal, R.; Sangamwar, A.T.; Jain, R. Synthesis, Biological Evaluation and 3D-QSAR Study of Hydrazide, Semicarbazide and Thiosemicarbazide Derivatives of 4-(Adamantan-1-Yl)Quinoline as Anti-Tuberculosis Agents. *Eur. J. Med. Chem.* **2014**, *85*, 255–267. [CrossRef] [PubMed]
20. Nagabushan, H.; Roopadevi, H.S. Bedaquiline: A Novel Antitubercular Drug for Multidrug-Resistant Tuberculosis. *J. Postgrad. Med.* **2014**, *60*, 300. [CrossRef] [PubMed]
21. Lee, H.; Ahn, S.; Hwang, N.Y.; Jeon, K.; Kwon, O.J.; Huh, H.J.; Lee, N.Y.; Kim, C.-K.; Koh, W.-J. Limited Effect of Later-Generation Fluoroquinolones in the Treatment of Ofloxacin-Resistant and Moxifloxacin-Susceptible Multidrug-Resistant Tuberculosis. *Antimicrob. Agents Chemother.* **2018**, *62*, e01784-17. [CrossRef] [PubMed]
22. Nie, Q.; Tao, L.; Li, Y.; Chen, N.; Chen, H.; Zhou, Y.; Wang, Y.; Chen, H.; Tang, Q.; Wang, X.; et al. High-Dose Gatifloxacin-Based Shorter Treatment Regimens for MDR/RR-TB. *Int. J. Infect. Dis.* **2022**, *115*, 142–148. [CrossRef]
23. Alós, J.-I. Quinolonas. *Enferm. Infec. Microbiol. Clínica* **2009**, *27*, 290–297. [CrossRef] [PubMed]
24. Joshi, S.D.; More, U.A.; Parkale, D.; Aminabhavi, T.M.; Gadad, A.K.; Nadagouda, M.N.; Jawarkar, R. Design, Synthesis of Quinolinylnyl Schiff Bases and Azetidines as Enoyl ACP-Reductase Inhibitors. *Med. Chem. Res.* **2015**, *24*, 3892–3911. [CrossRef]
25. Jain, P.P.; Degani, M.S.; Raju, A.; Anantram, A.; Seervi, M.; Sathaye, S.; Ray, M.; Rajan, M.G.R. Identification of a Novel Class of Quinoline–Oxadiazole Hybrids as Anti-Tuberculosis Agents. *Bioorg. Med. Chem. Lett.* **2016**, *26*, 645–649. [CrossRef] [PubMed]
26. Mandewale, M.C.; Thorat, B.; Nivid, Y.; Jadhav, R.; Nagarsekar, A.; Yamgar, R. Synthesis, Structural Studies and Antituberculosis Evaluation of New Hydrazone Derivatives of Quinoline and Their Zn(II) Complexes. *J. Saudi Chem. Soc.* **2018**, *22*, 218–228. [CrossRef]

27. Lindemann, A.; Patel, A.A.; Silver, N.L.; Tang, L.; Liu, Z.; Wang, L.; Tanaka, N.; Rao, X.; Takahashi, H.; Maduka, N.K.; et al. COTI-2, A Novel Thiosemicarbazone Derivative, Exhibits Antitumor Activity in HNSCC through P53-Dependent and -Independent Mechanisms. *Clin. Cancer Res.* **2019**, *25*, 5650–5662. [[CrossRef](#)] [[PubMed](#)]
28. Ibáñez-Escribano, A.; Fonseca-Berzal, C.; Martínez-Montiel, M.; Álvarez-Márquez, M.; Gómez-Núñez, M.; Lacueva-Arnedo, M.; Espinosa-Buitrago, T.; Martín-Pérez, T.; Escario, J.A.; Merino-Montiel, P.; et al. Thio- and Seleno-semicarbazones as Antiprotozoal Agents against *Trypanosoma Cruzi* and *Trichomonas Vaginalis*. *J. Enzym. Inhib. Med. Chem.* **2022**, *37*, 781–791. [[CrossRef](#)] [[PubMed](#)]
29. Hassan, M.; Ghaffari, R.; Sardari, S.; Farahani, Y.; Mohebbi, S. Discovery of Novel Isatin-Based Thiosemicarbazones: Synthesis, Antibacterial, Antifungal, and Antimycobacterial Screening. *Res. Pharm. Sci.* **2020**, *15*, 281. [[CrossRef](#)]
30. Souza, M.R.P.; Coelho, N.P.; Baldin, V.P.; Scodro, R.B.L.; Cardoso, R.F.; da Silva, C.C.; Vandresen, F. Synthesis of Novel (-)-Camphene-Based Thiosemicarbazones and Evaluation of Anti- *Mycobacterium Tuberculosis* Activity. *Nat. Prod. Res.* **2019**, *33*, 3372–3377. [[CrossRef](#)]
31. Beteck, R.M.; Seldon, R.; Jordaan, A.; Warner, D.F.; Hoppe, H.C.; Laming, D.; Khanye, S.D. New Quinolone-Based Thiosemicarbazones Showing Activity Against Plasmodium Falciparum and Mycobacterium Tuberculosis. *Molecules* **2019**, *24*, 1740. [[CrossRef](#)]
32. Volynets, G.P.; Tukalo, M.A.; Bdzhola, V.G.; Derkach, N.M.; Gumeniuk, M.I.; Tarnavskiy, S.S.; Starosyla, S.A.; Yarmoluk, S.M. Benzaldehyde Thiosemicarbazone Derivatives against Replicating and Nonreplicating Mycobacterium Tuberculosis. *J. Antibiot. (Tokyo)* **2019**, *72*, 218–224. [[CrossRef](#)]
33. Sens, L.; de Souza, A.C.A.; Pacheco, L.A.; Menegatti, A.C.O.; Mori, M.; Mascarello, A.; Nunes, R.J.; Terenzi, H. Synthetic Thiosemicarbazones as a New Class of Mycobacterium Tuberculosis Protein Tyrosine Phosphatase A Inhibitors. *Bioorg. Med. Chem.* **2018**, *26*, 5742–5750. [[CrossRef](#)] [[PubMed](#)]
34. Marvadi, S.K.; Krishna, V.S.; Surineni, G.; Srilakshmi Reshma, R.; Sridhar, B.; Sriram, D.; Kantevari, S. Synthesis, in Vitro, and in Vivo (Zebra Fish) Antitubercular Activity of 7,8-Dihydroquinolin-5(6H)-Ylidenehydrazinecarbothioamides. *Bioorganic Chem.* **2020**, *96*, 103626. [[CrossRef](#)] [[PubMed](#)]
35. Aziz, H.; Saeed, A.; Khan, M.A.; Afridi, S.; Jabeen, F.; Hashim, M. Novel N -Acyl-1 H -imidazole-1-carbothioamides: Design, Synthesis, Biological and Computational Studies. *Chem. Biodivers.* **2020**, *17*, e1900509. [[CrossRef](#)] [[PubMed](#)]
36. Salve, P.S.; Alegaon, S.G. Synthesis of New 7-Chloro-4-Phenoxyquinoline Analogues as Potential Antitubercular Agents. *Med. Chem. Res.* **2018**, *27*, 1–14. [[CrossRef](#)]
37. Matsa, R.; Makam, P.; Kaushik, M.; Hoti, S.L.; Kannan, T. Thiosemicarbazone Derivatives: Design, Synthesis and in Vitro Antimalarial Activity Studies. *Eur. J. Pharm. Sci.* **2019**, *137*, 104986. [[CrossRef](#)] [[PubMed](#)]
38. Shaik, A.B.; Bhandare, R.R.; Nissankararao, S.; Edis, Z.; Tangirala, N.R.; Shahanaaz, S.; Rahman, M.M. Design, Facile Synthesis and Characterization of Dichloro Substituted Chalcones and Dihydropyrazole Derivatives for Their Antifungal, Antitubercular and Antiproliferative Activities. *Molecules* **2020**, *25*, 3188. [[CrossRef](#)]
39. Hosny, N.M.; Hassan, N.Y.; Mahmoud, H.M.; Abdel-Rhman, M.H. Synthesis, Characterization and Cytotoxicity of New 2-isonicotinoyl-N-phenylhydrazine-1-carbothioamide and Its Metal Complexes. *Appl. Organomet. Chem.* **2019**, *33*, e4998. [[CrossRef](#)]
40. Elsaman, T.; Mohamed, M.S.; Mohamed, M.A. Current Development of 5-Nitrofuranyl Derivatives as Antitubercular Agents. *Bioorganic Chem.* **2019**, *88*, 102969. [[CrossRef](#)]
41. Cabrera, N.; Mora, J.R.; Márquez, E.; Flores-Morales, V.; Calle, L.; Cortés, E. QSAR and Molecular Docking Modelling of Anti-Leishmanial Activities of Organic Selenium and Tellurium Compounds. *SAR QSAR Environ. Res.* **2021**, *32*, 29–50. [[CrossRef](#)]
42. Kar, S.; Roy, K.; Leszczynski, J. Applicability Domain: A Step Toward Confident Predictions and Decidability for QSAR Modeling. In *Computational Toxicology*; Humana Press: New York, NY, USA, 2018.
43. Almi, I.; Belaidi, S.; Zerroug, E.; Alloui, M.; Ben Said, R.; Linguerrri, R.; Hochlaf, M. QSAR Investigations and Structure-Based Virtual Screening on a Series of Nitrobenzoxadiazole Derivatives Targeting Human Glutathione-S-Transferases. *J. Mol. Struct.* **2020**, *1211*, 128015. [[CrossRef](#)]
44. Hammoudi, N.-E.-H.; Sobhi, W.; Attoui, A.; Lemaoui, T.; Erto, A.; Benguerba, Y. In Silico Drug Discovery of Acetylcholinesterase and Butyrylcholinesterase Enzymes Inhibitors Based on Quantitative Structure-Activity Relationship (QSAR) and Drug-Likeness Evaluation. *J. Mol. Struct.* **2021**, *1229*, 129845. [[CrossRef](#)]
45. Golbraikh, A.; Tropsha, A. Predictive QSAR Modeling Based on Diversity Sampling of Experimental Datasets for the Training and Test Set Selection. *J. Comput. Aided Mol. Des.* **2002**, *16*, 357–369. [[CrossRef](#)] [[PubMed](#)]
46. Ertl, P. Cheminformatics Analysis of Organic Substituents: Identification of the Most Common Substituents, Calculation of Substituent Properties, and Automatic Identification of Drug-like Bioisosteric Groups. *J. Chem. Inf. Comput. Sci.* **2003**, *43*, 374–380. [[CrossRef](#)] [[PubMed](#)]
47. Lipinski, C.A.; Lombardo, F.; Dominy, B.W.; Feeney, P.J. Experimental and Computational Approaches to Estimate Solubility and Permeability in Drug Discovery and Development Settings. *Adv. Drug Deliv. Rev.* **1997**, *23*, 3–25. [[CrossRef](#)]
48. Cortes, E.; Mora, J.; Márquez, E. Modelling the Anti-Methicillin-Resistant Staphylococcus Aureus (MRSA) Activity of Cannabinoids: A QSAR and Docking Study. *Crystals* **2020**, *10*, 692. [[CrossRef](#)]
49. Cvetković, J.P.; Božić, B.Đ.; Banjac, N.R.; Petrović, J.; Soković, M.; Vitnik, V.D.; Vitnik, Ž.J.; Ušćumlić, G.S.; Valentić, N.V. Synthesis, Antimicrobial Activity and Quantum Chemical Investigation of Novel Succinimide Derivatives. *J. Mol. Struct.* **2019**, *1181*, 148–156. [[CrossRef](#)]

50. Eryılmaz, S.; Türk Çelikoğlu, E.; İdil, Ö.; İnkaya, E.; Kozak, Z.; Mısıır, E.; Gül, M. Derivatives of Pyridine and Thiazole Hybrid: Synthesis, DFT, Biological Evaluation via Antimicrobial and DNA Cleavage Activity. *Bioorganic Chem.* **2020**, *95*, 103476. [CrossRef]
51. Uzzaman, M.; Junaid, M.; Uddin, M.N. Evaluation of Anti-Tuberculosis Activity of Some Oxotitanium(IV) Schiff Base Complexes; Molecular Docking, Dynamics Simulation and ADMET Studies. *SN Appl. Sci.* **2020**, *2*, 880. [CrossRef]
52. Kumar, G.; Shankar, R. 2-Isoxazolines: A Synthetic and Medicinal Overview. *ChemMedChem* **2021**, *16*, 430–447. [CrossRef]
53. Zhang, G.; Chen, D.; Wang, S.; Chen, H.; Wei, N.; Chen, G. Molecular Insight into the Discrepancy of Antitubercular Activity between 8-Nitro and 8-Cyano Benzothiazinones. *Chem. Select* **2020**, *5*, 13775–13779. [CrossRef]
54. Al-Tamimi, A.-M.S.; Mary, Y.S.; Miniyar, P.B.; Al-Wahaibi, L.H.; El-Emam, A.A.; Armaković, S.; Armaković, S.J. Synthesis, Spectroscopic Analyses, Chemical Reactivity and Molecular Docking Study and Anti-Tubercular Activity of Pyrazine and Condensed Oxadiazole Derivatives. *J. Mol. Struct.* **2018**, *1164*, 459–469. [CrossRef]
55. Pitucha, M.; Karczmarzyk, Z.; Swatko-Ossor, M.; Drozd, M.; Wysocki, W.; Ginalska, G.; Urbanczyk-Lipkowska, Z.; Kowalczyk, D.; Morawiak, M. Synthesis and Structural Study of Some N-Acyl-4-Allylsemicarbazides and the Product of Their Cyclization with a Potential Antimicrobial Activity. *J. Mol. Struct.* **2020**, *1219*, 128552. [CrossRef]
56. Kucuk, C.; Yurdakul, S.; Erdem, B. Spectroscopic Characterization, DFT Calculations, and Microbiological Activity of 5-Iodoindole. *J. Mol. Struct.* **2022**, *1252*, 132125. [CrossRef]
57. Dubey, R.P.; Patel, U.H.; Pandya, S.B.; Chaudhary, K.P.; Socha, B.N. Cadmium Complex of Sulfathiazole Dihydrate with Secondary Ligand Pyridine: Structure, DFT Studies, Hirshfeld Surface Analysis and Antimicrobial Activity. *Indian J. Phys.* **2021**, *95*, 33–42. [CrossRef]
58. Lone, I.H.; Khan, K.Z.; Fozdar, B.I. Synthesis, Physicochemical Properties, Antimicrobial and Antioxidant Studies of Pyrazoline Derivatives Bearing a Pyridyl Moiety. *Med. Chem. Res.* **2014**, *23*, 363–369. [CrossRef]
59. Salim, A.S.; Girgis, A.S.; Basta, A.H.; El-saied, H.; Mohamed, M.A.; Bedair, A.H. Comparative DFT Computational Studies with Experimental Investigations for Novel Synthesized Fluorescent Pyrazoline Derivatives. *J. Fluoresc.* **2018**, *28*, 913–931. [CrossRef]
60. Lougheed, K.E.A.; Taylor, D.L.; Osborne, S.A.; Bryans, J.S.; Buxton, R.S. New Anti-Tuberculosis Agents Amongst Known Drugs. *Tuberc. Edinb. Scotl.* **2009**, *89*, 364. [CrossRef]
61. Patel, H.; Pawara, R.; Pawara, K.; Ahmed, F.; Shirkhedkar, A.; Surana, S. A Structural Insight of Bedaquiline for the Cardiotoxicity and Hepatotoxicity. *Tuberculosis* **2019**, *117*, 79–84. [CrossRef]
62. Ahmad, I.; Jadhav, H.; Shinde, Y.; Jagtap, V.; Girase, R.; Patel, H. Optimizing Bedaquiline for Cardiotoxicity by Structure Based Virtual Screening, DFT Analysis and Molecular Dynamic Simulation Studies to Identify Selective MDR-TB Inhibitors. *Silico Pharmacol.* **2021**, *9*. [CrossRef]
63. Aldred, K.J.; Blower, T.R.; Kerns, R.J.; Berger, J.M.; Osherooff, N. Fluoroquinolone Interactions with Mycobacterium Tuberculosis Gyrase: Enhancing Drug Activity against Wild-Type and Resistant Gyrase. *Proc. Natl. Acad. Sci. USA* **2016**, *113*, E839–E846. [CrossRef]
64. Sarathy, J.; Blanc, L.; Alvarez-Cabrera, N.; O'Brien, P.; Dias-Freedman, I.; Mina, M.; Zimmerman, M.; Kaya, F.; Ho Liang, H.-P.; Prideaux, B.; et al. Fluoroquinolone Efficacy against Tuberculosis Is Driven by Penetration into Lesions and Activity against Resident Bacterial Populations. *Antimicrob. Agents Chemother.* **2019**, *63*, e02516-18. [CrossRef] [PubMed]
65. Antimicrobial and Anti-Tubercular Activity of Quinolone Analogues. Available online: <https://scialert.net/abstract/?doi=sciintl.2013.336.349> (accessed on 5 December 2022).
66. Hotra, A.; Ragonathan, P.; Ng, P.S.; Seankongsuk, P.; Harikishore, A.; Sarathy, J.P.; Saw, W.-G.; Lakshmanan, U.; Sae-Lao, P.; Kalia, N.P.; et al. Discovery of a Novel Mycobacterial F-ATP Synthase Inhibitor and Its Potency in Combination with Diarylquinolines. *Angew. Chem. Int. Ed.* **2020**, *59*, 13295–13304. [CrossRef]
67. Richter, A.; Rudolph, I.; Möllmann, U.; Voigt, K.; Chung, C.W.; Singh, O.M.P.; Rees, M.; Mendoza-Losana, A.; Bates, R.; Ballell, L.; et al. Novel Insight into the Reaction of Nitro, Nitroso and Hydroxylamino Benzothiazinones and of Benzoxacinones with Mycobacterium Tuberculosis DprE1. *Sci. Rep.* **2018**, *8*, 13473. [CrossRef] [PubMed]
68. Ali, M.T.; Blicharska, N.; Shilpi, J.A.; Seidel, V. Investigation of the Anti-TB Potential of Selected Propolis Constituents Using a Molecular Docking Approach. *Sci. Rep.* **2018**, *8*, 1–8. [CrossRef] [PubMed]
69. Wang, H.; Jiang, M.; Sun, F.; Li, S.; Hse, C.-Y.; Jin, C. Screening, Synthesis, and QSAR Research on Cinnamaldehyde-Amino Acid Schiff Base Compounds as Antibacterial Agents. *Molecules* **2018**, *23*, 3027. [CrossRef]
70. Upadhyay, H.C.; Singh, M.; Prakash, O.; Khan, F.; Srivastava, S.K.; Bawankule, D.U. QSAR, ADME and Docking Guided Semi-Synthesis and in Vitro Evaluation of 4-Hydroxy- α -Tetralone Analogs for Anti-Inflammatory Activity. *SN Appl. Sci.* **2020**, *2*, 2069. [CrossRef]
71. Jin, Y.; Fan, S.; Lv, G.; Meng, H.; Sun, Z.; Jiang, W.; Van Lanen, S.G.; Yang, Z. Computer-Aided Drug Design of Capuramycin Analogues as Anti-Tuberculosis Antibiotics by 3D-QSAR and Molecular Docking. *Open Chem.* **2017**, *15*, 299–307. [CrossRef]
72. Saxena, M.; Gaur, S.; Prathipati, P.; Saxena, A.K. Synthesis of Some Substituted Pyrazinopyridoindoles and 3D QSAR Studies along with Related Compounds: Piperazines, Piperidines, Pyrazinoisoquinolines, and Diphenhydramine, and Its Semi-Rigid Analogs as Antihistamines (H1). *Bioorg. Med. Chem.* **2006**, *14*, 8249–8258. [CrossRef]
73. Meth-Cohn, O.; Narine, B.; Tarnowski, B. A Versatile New Synthesis of Quinolines and Related Fused Pyridines, Part 5. The Synthesis of 2-Chloroquinoline-3-Carbaldehydes. *J. Chem. Soc. Perkin.* **1981**, *1*, 15250. [CrossRef]
74. Abonia, R.; Insuasty, D.; Castillo, J.; Insuasty, B.; Quiroga, J.; Nogueras, M.; Cobo, J. Synthesis of Novel Quinoline-2-One Based Chalcones of Potential Anti-Tumor Activity. *Eur. J. Med. Chem.* **2012**, *57*, 29–40. [CrossRef]

75. Brudey, K.; Driscoll, J.R.; Rigouts, L.; Prodinger, W.M.; Gori, A.; Al-Hajoj, S.A.; Allix, C.; Aristimuño, L.; Arora, J.; Baumanis, V.; et al. Mycobacterium Tuberculosis Complex Genetic Diversity: Mining the Fourth International Spoligotyping Database (SpolDB4) for Classification, Population Genetics and Epidemiology. *BMC Microbiol.* **2006**, *6*, 23. [CrossRef] [PubMed]
76. Glynn, J. Beijing/W Genotype Mycobacterium Tuberculosis and Drug Resistance—PubMed. Available online: <https://pubmed.ncbi.nlm.nih.gov/16704829/> (accessed on 29 June 2022).
77. Reynaud, Y.; Millet, J.; Rastogi, N. Genetic Structuration, Demography and Evolutionary History of Mycobacterium Tuberculosis LAM9 Sublineage in the Americas as Two Distinct Subpopulations Revealed by Bayesian Analyses. *PLoS ONE* **2015**, *10*, e0140911. [CrossRef] [PubMed]
78. Cubillos-Ruiz, A.; Sandoval, A.; Ritacco, V.; López, B.; Robledo, J.; Correa, N.; Hernandez-Neuta, I.; Zambrano, M.M.; Del Portillo, P. Genomic Signatures of the Haarlem Lineage of Mycobacterium Tuberculosis: Implications of Strain Genetic Variation in Drug and Vaccine Development. *J. Clin. Microbiol.* **2010**, *48*, 3614–3623. [CrossRef] [PubMed]
79. Fourches, D.; Muratov, E.; Tropsha, A. Trust, but Verify II: A Practical Guide to Chemogenomics Data Curation. *J. Chem. Inf. Model.* **2016**, *56*, 1243–1252. [CrossRef] [PubMed]
80. Fourches, D.; Muratov, E.; Tropsha, A. Trust, But Verify: On the Importance of Chemical Structure Curation in Cheminformatics and QSAR Modeling Research. *J. Chem. Inf. Model.* **2010**, *50*, 1189–1204. [CrossRef]
81. Tropsha, A.; Bajorath, J. Computational Methods for Drug Discovery and Design. *J. Med. Chem.* **2016**, *59*, 1. [CrossRef]
82. Cherkasov, A.; Muratov, E.N.; Fourches, D.; Varnek, A.; Baskin, I.I.; Cronin, M.; Dearden, J.; Gramatica, P.; Martin, Y.C.; Todeschini, R.; et al. QSAR Modeling: Where Have You Been? Where Are You Going To? *J. Med. Chem.* **2014**, *57*, 4977–5010. [CrossRef]
83. Mandewale, M.C.; Thorat, B.; Shelke, D.; Yamgar, R. Synthesis and Biological Evaluation of New Hydrazone Derivatives of Quinoline and Their Cu(II) and Zn(II) Complexes against *Mycobacterium Tuberculosis*. *Bioinorg. Chem. Appl.* **2015**, *2015*. [CrossRef]
84. Patel, D.B.; Darji, D.G.; Patel, K.R.; Rajani, D.P.; Rajani, S.D.; Patel, H.D. Synthesis of Novel Quinoline-thiosemicarbazide Hybrids and Evaluation of Their Biological Activities, Molecular Docking, Molecular Dynamics, Pharmacophore Model Studies, and ADME-Tox Properties. *J. Heterocycl. Chem.* **2020**, *57*. [CrossRef]
85. Salve, P.S.; Alegaon, S.G.; Sriram, D. Three-Component, One-Pot Synthesis of Anthranilamide Schiff Bases Bearing 4-Aminoquinoline Moiety as Mycobacterium Tuberculosis Gyrase Inhibitors. *Bioorg. Med. Chem. Lett.* **2017**, *27*. [CrossRef]
86. Wolf, A.; Shahid, M.; Kasam, V.; Ziegler, W.; Hofmann-Apitius, M. In Silico Drug Discovery Approaches on Grid Computing Infrastructures. *Curr. Clin. Pharmacol.* **2010**, *5*, 37–46. [CrossRef] [PubMed]
87. Insuasty, D.; Vidal, O.; Bernal, A.; Marquez, E.; Guzman, J.; Insuasty, B.; Quiroga, J.; Svetaz, L.; Zacchino, S.; Puerto, G.; et al. Antimicrobial Activity of Quinoline-Based Hydroxyimidazolium Hybrids. *Antibiotics* **2019**, *8*, 239. [CrossRef] [PubMed]
88. Thomas, K.D.; Adhikari, A.V.; Telkar, S.; Chowdhury, I.H.; Mahmood, R.; Pal, N.K.; Row, G.; Sumesh, E. Design, Synthesis and Docking Studies of New Quinoline-3-Carbohydrazide Derivatives as Antitubercular Agents. *Eur. J. Med. Chem.* **2011**, *46*, 5283–5292. [CrossRef] [PubMed]
89. Yuanita, E.; Dharmayani, N.K.T.; YUlfa, M.; Syahri, J. Quantitative Structure–Activity Relationship (QSAR) and Molecular Docking of Xanthone Derivatives as Anti-Tuberculosis Agents. *J. Clin. Tuberc. Mycobact. Dis.* **2020**, *21*, 100203. [CrossRef]
90. Adeniji, S.E.; Adamu Shallangwa, G.; Ebuka Arthur, D.; Abdullahi, M.; Mahmoud, A.Y.; Haruna, A. Quantum Modelling and Molecular Docking Evaluation of Some Selected Quinoline Derivatives as Anti-Tubercular Agents. *Heliyon* **2020**, *6*, e03639. [CrossRef] [PubMed]
91. Mali, S.N.; Pandey, A.; Thorat, B.R.; Lai, C.-H. Multiple 3D- and 2D-Quantitative Structure–Activity Relationship Models (QSAR), Theoretical Study and Molecular Modeling to Identify Structural Requirements of Imidazopyridine Analogues as Anti-Infective Agents against Tuberculosis. *Struct. Chem.* **2022**, *33*, 679–694. [CrossRef]
92. Aher, R.B.; Sarkar, D. 2D-QSAR Modeling and Two-Fold Classification of 1,2,4-Triazole Derivatives for Antitubercular Potency against the Dormant Stage of Mycobacterium Tuberculosis. *Mol. Divers.* **2022**, *26*, 1227–1242. [CrossRef] [PubMed]
93. Nayyar, A.; Malde, A.; Coutinho, E.; Jain, R. Synthesis, Anti-Tuberculosis Activity, and 3D-QSAR Study of Ring-Substituted-2/4-Quinolinecarbaldehyde Derivatives. *Bioorg. Med. Chem.* **2006**, *14*, 7302–7310. [CrossRef]
94. Hosseini, S.; Ketabi, S.; Hasheminasab, G. QSAR Study of Antituberculosis Activity of Oxadiazole Derivatives Using DFT Calculations. *J. Recept. Signal Transduct.* **2022**, *42*, 503–511. [CrossRef]
95. Alam, S.; Khan, F. 3D-QSAR Studies on Maslinic Acid Analogs for Anticancer Activity against Breast Cancer Cell Line MCF-7. *Sci. Rep.* **2017**, *7*, 6019. [CrossRef]
96. Abdel-Aziz, H.; Eldehna, W.; Fares, M.; Al-Rashood, S.; Al-Rashood, K.; Abdel-Aziz, M.; Soliman, D. Synthesis, Biological Evaluation and 2D-QSAR Study of Halophenyl Bis-Hydrazones as Antimicrobial and Antitubercular Agents. *Int. J. Mol. Sci.* **2015**, *16*, 8719–8743. [CrossRef] [PubMed]
97. Hanwell, M.D.; Curtis, D.E.; Lonie, D.C.; Vandermeersch, T.; Zurek, E.; Hutchison, G.R. Avogadro: An Advanced Semantic Chemical Editor, Visualization, and Analysis Platform. *J. Cheminformatics* **2012**, *4*, 2946–2954. [CrossRef] [PubMed]
98. Frisch, M.J.; Trucks, G.W.; Schlegel, H.B.; Scuseria, G.E.; Robb, M.A.; Cheeseman, J.R.; Scalmani, G.; Barone, V.; Mennucci, B.; Petersson, G.A.; et al. *Gaussian 09, Revision, D.01*; Gaussian Inc.: Wallingford Center, CT, USA, 2009.
99. Mahmud, A.W.; Shallangwa, G.A.; Uzairu, A. QSAR and Molecular Docking Studies of 1,3-Dioxoisindoline-4-Aminoquinolines as Potent Antiplasmodium Hybrid Compounds. *Heliyon* **2020**, *6*. [CrossRef] [PubMed]

100. Oyewole, R.O.; Oyebamiji, A.K.; Semire, B. Theoretical Calculations of Molecular Descriptors for Anticancer Activities of 1, 2, 3-Triazole-Pyrimidine Derivatives against Gastric Cancer Cell Line (MGC-803): DFT, QSAR and Docking Approaches. *Heliyon* **2020**, *6*. [[CrossRef](#)]
101. Appell, M.; Tu, Y.-S.; Compton, D.L.; Evans, K.O.; Wang, L.C. Quantitative Structure-Activity Relationship Study for Prediction of Antifungal Properties of Phenolic Compounds. *Struct. Chem.* **2020**, *31*, 1621–1630. [[CrossRef](#)]
102. Adeniji, S.E.; Arthur, D.E.; Oluwaseye, A. Computational Modeling of 4-Phenoxy nicotinamide and 4-Phenoxy pyrimidine-5-Carboxamide Derivatives as Potent Anti-Diabetic Agent against TGR5 Receptor. *J. King Saud Univ. Sci.* **2020**, *32*, 102–115. [[CrossRef](#)]
103. Saad, F.A.; El-Metwaly, N.M.; Farghaly, T.A.; Elghalban, M.G.; Shah, R.K.; Al-Hazmi, G.A.; Saleh, K.A.; Alfaifi, M.Y. Illustration for Series of New Metal Ion Complexes Extracted from Pyrazolone Derivative, Spectral, Thermal, QSAR, DFT/B3LYP, Docking and Antitumor Investigations. *J. Mol. Liq.* **2017**, *229*. [[CrossRef](#)]
104. Djeradi, H.; Rahmouni, A.; Cheriti, A. Antioxidant Activity of Flavonoids: A QSAR Modeling Using Fukui Indices Descriptors. *J. Mol. Model.* **2014**, *20*, 614–627. [[CrossRef](#)]
105. Horst, B. Molecular Descriptors and the Electronic Structure. In *Statistical Modelling of Molecular Descriptors in QSAR/QSPR*; Wiley-VCH Verlag GmbH & Co. KGaA: Weinheim, Germany, 2012.
106. Naef, R.; Acree, W. Calculation of Five Thermodynamic Molecular Descriptors by Means of a General Computer Algorithm Based on the Group-Additivity Method: Standard Enthalpies of Vaporization, Sublimation and Solvation, and Entropy of Fusion of Ordinary Organic Molecules and Total Phase-Change Entropy of Liquid Crystals. *Molecules* **2017**, *22*, 1059. [[CrossRef](#)]
107. Yoshimori, A. Prediction of Molecular Properties Using Molecular Topographic Map. *Molecules* **2021**, *26*, 4475. [[CrossRef](#)]
108. Geerlings, P.; De Proft, F.; Langenaeker, W. Conceptual Density Functional Theory. *Chem. Rev.* **2003**, *103*, 1793–1874. [[CrossRef](#)] [[PubMed](#)]
109. Zanni, R.; Galvez-Llompарт, M.; Garcia-Domenech, R.; Galvez, J. What Place Does Molecular Topology Have in Today's Drug Discovery? *Expert Opin. Drug Discov.* **2020**, *15*, 1133–1144. [[CrossRef](#)] [[PubMed](#)]
110. García-Jacas, C.R.; Marrero-Ponce, Y.; Vivas-Reyes, R.; Suárez-Lezcano, J.; Martínez-Rios, F.; Terán, J.E.; Aguilera-Mendoza, L. Distributed and Multicore QuBiLS-MIDAS Software v2.0: Computing Chiral, Fuzzy, Weighted and Truncated Geometrical Molecular Descriptors Based on Tensor Algebra. *J. Comput. Chem.* **2020**, *41*, 1209–1227. [[CrossRef](#)] [[PubMed](#)]
111. Heinze, G.; Wallisch, C.; Dunkler, D. Variable Selection—A Review and Recommendations for the Practicing Statistician. *Biom. J.* **2018**, *60*. [[CrossRef](#)]
112. Gramatica, P. Principles of QSAR Models Validation: Internal and External. *QSAR Comb. Sci.* **2007**, *26*, 694–701. [[CrossRef](#)]
113. Cramer, R.D.; Bunce, J.D.; Patterson, D.E.; Frank, I.E. Crossvalidation, Bootstrapping, and Partial Least Squares Compared with Multiple Regression in Conventional QSAR Studies. *Quant. Struct.-Act. Relatsh.* **1988**, *7*, 18–25. [[CrossRef](#)]
114. Rücker, C.; Rücker, G.; Meringer, M. Y-Randomization and Its Variants in QSPR/QSAR. *J. Chem. Inf. Model.* **2007**, *47*, 2345–2357. [[CrossRef](#)]
115. Golbraikh, A.; Tropsha, A. Beware of Q²! *J. Mol. Graph. Model.* **2002**, *20*, 269–276. [[CrossRef](#)]
116. Forli, S.; Huey, R.; Pique, M.E.; Sanner, M.F.; Goodsell, D.S.; Olson, A.J. Computational Protein–Ligand Docking and Virtual Drug Screening with the AutoDock Suite. *Nat. Protoc.* **2016**, *11*, 905–919. [[CrossRef](#)]
117. Pradeep Kumar, C.B.; Prathibha, B.S.; Prasad, K.N.N.; Raghu, M.S.; Prashanth, M.K.; Jayanna, B.K.; Alharthi, F.A.; Chandrasekhar, S.; Revanasiddappa, H.D.; Yogesh Kumar, K. Click Synthesis of 1,2,3-Triazole Based Imidazoles: Antitubercular Evaluation, Molecular Docking and HSA Binding Studies. *Bioorg. Med. Chem. Lett.* **2021**, *36*, 127810. [[CrossRef](#)]
118. Danne, A.B.; Choudhari, A.S.; Chakraborty, S.; Sarkar, D.; Khedkar, V.M.; Shingate, B.B. Triazole–Diindolylmethane Conjugates as New Antitubercular Agents: Synthesis, Bioevaluation, and Molecular Docking. *MedChemComm* **2018**, *9*, 1114–1130. [[CrossRef](#)] [[PubMed](#)]
119. Naz, S.; Farooq, U.; Khan, S.; Sarwar, R.; Mabkhot, Y.N.; Saeed, M.; Alsayari, A.; Muhsinah, A.; Bin Ul-Haq, Z. Pharmacophore Model-Based Virtual Screening, Docking, Biological Evaluation and Molecular Dynamics Simulations for Inhibitors Discovery against α -Tryptophan Synthase from Mycobacterium Tuberculosis. *J. Biomol. Struct. Dyn.* **2020**, *39*, 610–620. [[CrossRef](#)] [[PubMed](#)]
120. Das, N.; Jena, P.K.; Pradhan, S.K. Arabinosyltransferase C Enzyme of Mycobacterium Tuberculosis, a Potential Drug Target: An Insight from Molecular Docking Study. *Heliyon* **2020**, *6*, e02693. [[CrossRef](#)] [[PubMed](#)]
121. Khedr, M.A.; Pillay, M.; Chandrashekarappa, S.; Chopra, D.; Aldhubiab, B.E.; Attimarad, M.; Alwassil, O.I.; Mlisana, K.; Odhav, B.; Venugopala, K.N. Molecular Modeling Studies and Anti-TB Activity of Trisubstituted Indolizine Analogues; Molecular Docking and Dynamic Inputs. *J. Biomol. Struct. Dyn.* **2017**, *36*, 2163–2178. [[CrossRef](#)]
122. Holas, O.; Ondrejcek, P.; Dolezal, M. Mycobacterium Tuberculosis Enoyl-Acyl Carrier Protein Reductase Inhibitors as Potential Antituberculars: Development in the Past Decade. *J. Enzym. Inhib. Med. Chem.* **2015**, *30*, 629–648. [[CrossRef](#)]
123. Mahapatra, S.; Woolhiser, L.K.; Lenaerts, A.J.; Johnson, J.L.; Eisenach, K.D.; Joloba, M.L.; Boom, W.H.; Belisle, J.T. A Novel Metabolite of Antituberculosis Therapy Demonstrates Host Activation of Isoniazid and Formation of the Isoniazid-NAD + Adduct. *Antimicrob. Agents Chemother.* **2012**, *56*, 28–35. [[CrossRef](#)]
124. Chikhale, R.V.; Barmade, M.A.; Murumkar, P.R.; Yadav, M.R. Overview of the Development of DprE1 Inhibitors for Combating the Menace of Tuberculosis. *J. Med. Chem.* **2018**, *61*, 8563–8593. [[CrossRef](#)]
125. Oleg, T.; Arthur, J.O. AutoDock Vina: Improving the Speed and Accuracy of Docking with a New Scoring Function, Efficient Optimization, and Multithreading. *J. Comput. Chem.* **2010**, *31*, 455–461. [[CrossRef](#)]

126. Kumari, R.; Kumar, R.; Lynn, A. G-Mmpbsa -A GROMACS Tool for High-Throughput MM-PBSA Calculations. *J. Chem. Inf. Model.* **2014**, *54*, 1951–1962. [[CrossRef](#)]
127. Lindorff-Larsen, K.; Piana, S.; Palmo, K.; Maragakis, P.; Klepeis, J.L.; Dror, R.O.; Shaw, D.E. Improved Side-Chain Torsion Potentials for the Amber Ff99SB Protein Force Field. *Proteins Struct. Funct. Bioinforma.* **2010**, *78*, 1950–1958. [[CrossRef](#)]
128. Sousa da Silva, A.W.; Vranken, W.F. ACPYPE—AnteChamber PYthon Parser InterfacE. *BMC Res. Notes* **2012**, *5*, 367. [[CrossRef](#)] [[PubMed](#)]
129. Carloni, P.; Rothlisberger, U.; Parrinello, M. The Role and Perspective of Ab Initio Molecular Dynamics in the Study of Biological Systems. *Acc. Chem. Res.* **2002**, *35*, 455–464. [[CrossRef](#)] [[PubMed](#)]
130. Christensen, A.S.; Kubař, T.; Cui, Q.; Elstner, M. Semiempirical Quantum Mechanical Methods for Noncovalent Interactions for Chemical and Biochemical Applications. *Chem. Rev.* **2016**, *116*, 5301–5337. [[CrossRef](#)] [[PubMed](#)]
131. Faver, J.; Merz, K.M. The Utility of the HSAB Principle via the Fukui Function in Biological Systems. *J. Chem. Theory Comput.* **2010**, *6*, 548–559. [[CrossRef](#)] [[PubMed](#)]
132. Lu, Y.; Wang, Y.; Zhu, W. Nonbonding Interactions of Organic Halogens in Biological Systems: Implications for Drug Discovery and Biomolecular Design. *Phys. Chem. Chem. Phys.* **2010**, *12*, 4543–4551. [[CrossRef](#)] [[PubMed](#)]
133. Rocha-Santos, A.; Chaves, E.J.F.; Grillo, I.B.; de Freitas, A.S.; Araújo, D.A.M.; Rocha, G.B. Thermochemical and Quantum Descriptor Calculations for Gaining Insight into Ricin Toxin A (RTA) Inhibitors. *ACS Omega* **2021**, *6*, 8764–8777. [[CrossRef](#)]
134. Sapse, A.-M. (Ed.) *Molecular Orbital Calculations for Biological Systems*; Topics in Physical Chemistry; Oxford University Press: New York, NY, USA, 1998; ISBN 978-0-19-509873-0.
135. Stachowicz, J.; Krajewska-Kulak, E.; Lukaszuk, C.; Niewiadomy, A. Relationship between Antifungal Activity against *Candida Albicans* and Electron Parameters of Selected N-Heterocyclic Thioamides. *Indian J. Pharm. Sci.* **2014**, *76*, 287.
136. Tanaka, S.; Mochizuki, Y.; Komeiji, Y.; Okiyama, Y.; Fukuzawa, K. Electron-Correlated Fragment-Molecular-Orbital Calculations for Biomolecular and Nano Systems. *Phys. Chem. Chem. Phys.* **2014**, *16*, 10310–10344. [[CrossRef](#)]
137. Zhao, Y.; Truhlar, D.G. How Well Can New-Generation Density Functional Methods Describe Stacking Interactions in Biological Systems? *Phys. Chem. Chem. Phys.* **2005**, *7*, 2701–2705. [[CrossRef](#)]
138. Suarez, M.; Valencia, J.; Cadena, C.; Maiti, R.; Datta, C.; Puerto, G.; Isaza, J.; San Juan, H.; Nagaraja, V.; Guzman, J. Diarylethenes Display In Vitro Anti-TB Activity and Are Efficient Hits Targeting the Mycobacterium Tuberculosis HU Protein. *Molecules* **2017**, *22*, 1245. [[CrossRef](#)]

Disclaimer/Publisher’s Note: The statements, opinions and data contained in all publications are solely those of the individual author(s) and contributor(s) and not of MDPI and/or the editor(s). MDPI and/or the editor(s) disclaim responsibility for any injury to people or property resulting from any ideas, methods, instructions or products referred to in the content.